

# $\mu_*$ masses: weak-lensing calibration of the Dark Energy Survey Year 1 redMaPPer clusters using stellar masses

M. E. S. Pereira,<sup>1</sup> A. Palmese,<sup>2,3</sup> T. N. Varga,<sup>4,5</sup> T. McClintock,<sup>6</sup> M. Soares-Santos,<sup>1</sup> J. Burgad,<sup>7</sup> J. Annis,<sup>2</sup> A. Farahi,<sup>8</sup> H. Lin,<sup>2</sup> A. Choi,<sup>9</sup> J. DeRose,<sup>10,11</sup> J. Esteves,<sup>1</sup> M. Gatti,<sup>12</sup> D. Gruen,<sup>13,14,15</sup> W. G. Hartley,<sup>16,17,18</sup> B. Hoyle,<sup>4,5</sup> T. Jeltema,<sup>11</sup> N. MacCrann,<sup>9,19</sup> A. Roodman,<sup>14,15</sup> C. Sánchez,<sup>20</sup> T. Shin,<sup>20</sup> A. von der Linden,<sup>21</sup> J. Zuntz,<sup>22</sup> T. M. C. Abbott,<sup>23</sup> M. Aguena,<sup>24,25</sup> S. Avila,<sup>26</sup> E. Bertin,<sup>27,28</sup> S. Bhargava,<sup>29</sup> S. L. Bridle,<sup>30</sup> D. Brooks,<sup>17</sup> D. L. Burke,<sup>14,15</sup> A. Carnero Rosell,<sup>31,32</sup> M. Carrasco Kind,<sup>33,34</sup> J. Carretero,<sup>12</sup> M. Costanzi,<sup>35,36</sup> L. N. da Costa,<sup>25,37</sup> S. Desai,<sup>38</sup> H. T. Diehl,<sup>2</sup> J. P. Dietrich,<sup>39</sup> P. Doel,<sup>17</sup> J. Estrada,<sup>2</sup> S. Everett,<sup>11</sup> B. Flaugher,<sup>2</sup> P. Fosalba,<sup>40,41</sup> J. Frieman,<sup>2,3</sup> J. García-Bellido,<sup>26</sup> E. Gaztanaga,<sup>40,41</sup> D. W. Gerdes,<sup>8,42</sup> R. A. Gruendl,<sup>33,34</sup> J. Gschwend,<sup>25,37</sup> G. Gutierrez,<sup>2</sup> S. R. Hinton,<sup>43</sup> D. L. Hollowood,<sup>11</sup> K. Honscheid,<sup>9,19</sup> D. J. James,<sup>44</sup> K. Kuehn,<sup>45,46</sup> N. Kuropatkin,<sup>2</sup> O. Lahav,<sup>17</sup> M. Lima,<sup>24,25</sup> M. A. G. Maia,<sup>25,37</sup> M. March,<sup>20</sup> J. L. Marshall,<sup>47</sup> P. Melchior,<sup>48</sup> F. Menanteau,<sup>33,34</sup> R. Miquel,<sup>12,49</sup> R. L. C. Ogando,<sup>25,37</sup> F. Paz-Chinchón,<sup>34,50</sup> A. A. Plazas,<sup>48</sup> A. K. Romer,<sup>29</sup> E. Sanchez,<sup>51</sup> V. Scarpine,<sup>2</sup> M. Schubnell,<sup>8</sup> S. Serrano,<sup>40,41</sup> I. Sevilla-Noarbe,<sup>51</sup> M. Smith,<sup>52</sup> E. Suchyta,<sup>53</sup> M. E. C. Swanson,<sup>34</sup> G. Tarle,<sup>8</sup> R. H. Wechsler,<sup>13,14,15</sup> J. Weller,<sup>4,5</sup> and Y. Zhang<sup>2</sup>  
(DES Collaboration)

*Affiliations are listed at the end of the paper*

Accepted 2020 August 31. Received 2020 August 14; in original form 2020 June 18

## ABSTRACT

We present the weak-lensing mass calibration of the stellar-mass-based  $\mu_*$  mass proxy for redMaPPer galaxy clusters in the Dark Energy Survey Year 1. For the first time, we are able to perform a calibration of  $\mu_*$  at high redshifts,  $z > 0.33$ . In a blinded analysis, we use  $\sim 6000$  clusters split into 12 subsets spanning the ranges  $0.1 \leq z < 0.65$  and  $\mu_*$  up to  $\sim 5.5 \times 10^{13} M_\odot$ , and infer the average masses of these subsets through modelling of their stacked weak-lensing signal. In our model, we account for the following sources of systematic uncertainty: shear measurement and photometric redshift errors, miscentring, cluster-member contamination of the source sample, deviations from the Navarro–Frenk–White halo profile, halo triaxiality, and projection effects. We use the inferred masses to estimate the joint mass– $\mu_*$ – $z$  scaling relation given by  $\langle M_{200c} | \mu_*, z \rangle = M_0(\mu_*/5.16 \times 10^{12} M_\odot)^{F_{\mu_*}}((1+z)/1.35)^{G_z}$ . We find  $M_0 = (1.14 \pm 0.07) \times 10^{14} M_\odot$  with  $F_{\mu_*} = 0.76 \pm 0.06$  and  $G_z = -1.14 \pm 0.37$ . We discuss the use of  $\mu_*$  as a complementary mass proxy to the well-studied richness  $\lambda$  for: (i) exploring the regimes of low  $z$ ,  $\lambda < 20$  and high  $\lambda$ ,  $z \sim 1$ ; and (ii) testing systematics such as projection effects for applications in cluster cosmology.

**Key words:** gravitational lensing: weak – galaxies: clusters: general – cosmology: observations.

## 1 INTRODUCTION

Galaxy clusters are an important tool for studying the formation and evolution of structure in the Universe, the distribution of matter, and for testing modified gravity models. The count of galaxy clusters as a function of mass and redshift is potentially one of the most powerful cosmological probes (Haiman, Mohr & Holder 2001; Voit 2005; Allen, Evrard & Mantz 2011; Kravtsov & Borgani 2012; Ettori & Meneghetti 2013; Penna-Lima, Makler & Wuensche 2014; Harvey et al. 2015; Dodelson et al. 2016). In order to achieve this potential, it is necessary to understand and correct for the systematics involved

in the cluster mass calibration, which is currently the dominating source of uncertainties for using clusters to probe cosmology (Rozo et al. 2010; Mantz et al. 2015; Planck Collaboration XXIV 2016; Costanzi et al. 2019a; Murata et al. 2019; DES Collaboration 2020).

Galaxy clusters act as powerful gravitational lenses because their large gravitational fields produce distortions in the shape of the background galaxies. This effect does not depend on the dynamical state of the cluster (as does the X-ray luminosity) and is sensitive to all of its matter content (both baryonic and dark matter). Therefore, using this effect we can assess their matter content and perform very precise mass measurements. Only the most massive clusters have weak-lensing signals sufficiently strong to be individually measured in the current generation of wide-field surveys. Thus, we combine the

\* E-mail: elidaiana.sp@gmail.com (MESP); palmese@fnal.gov (AP)

lensing signal of a large number of clusters with similar properties (i.e. *stacking*) to obtain measurements of higher signal-to-noise.

In practice, we can rank the clusters by some proxy for the mass and, then, use the weak-lensing effect to have an estimate of the total halo mass. Thus, a mass–observable relation (MOR) must be calibrated to connect the observable and the total halo mass. The technique of stacking the weak-lensing signal of many systems in a given observable interval provides one of the most direct and model-independent methods to calibrate the MORs. The community has made a concerted effort to determine the scaling relations empirically (Sheldon et al. 2001; Johnston et al. 2007; Applegate et al. 2014; Oguri 2014; von der Linden et al. 2014a, b; Ford et al. 2015; Hoekstra et al. 2015; Mantz et al. 2015; Wen & Han 2015; Wiesner, Lin & Soares-Santos 2015; Okabe & Smith 2016; Melchior et al. 2017; Simet et al. 2017; Medezinski et al. 2018; Murata et al. 2018, 2019; Pereira et al. 2018; Bellagamba et al. 2019; Dietrich et al. 2019; McClintock et al. 2019; Miyatake et al. 2019). The MORs are not the same for these cluster samples and mass proxies. However, one should expect the cosmological constraints from using these different MORs to be consistent.

Currently, the state-of-the-art mass calibration of optically selected clusters is performed by the Dark Energy Survey (DES) with cluster catalogues from the redMaPPer cluster finder (Rykoff et al. 2014, 2016), using the optical count of red galaxies,  $\lambda$ , as the mass proxy, and DES shear catalogues for the weak-lensing mass calibration. The red galaxy count  $\lambda$  (aka ‘richness’) is computed as the sum of the membership probabilities of red galaxies within a cluster-scale radius and brighter than some luminosity threshold, where the membership probabilities are assigned based on a model for the red sequence as a function of the redshifts ( $z$ ) and on a radial filter. In the most recent result from McClintock et al. (2019) with the DES Year 1 (Y1) data, the mass calibration was performed in the range of  $0.2 < z < 0.65$  and  $\lambda > 20$ . For the last analysis with the DES Y1 through Year 6 (Y6) data, we expect to have a cluster sample going to  $z \sim 1$ .

The key assumption that redMaPPer uses to identify clusters is that each cluster has a well-defined red-sequence population. At low redshifts, this is a powerful assumption and allows efficient cluster finding. It is unclear at what redshift all clusters gain a red sequence. The evolution of the red sequence is still a topic of considerable debate (Brammer et al. 2009; Sommariva et al. 2014; Feldmann et al. 2016; Cecchi et al. 2019; Girelli, Bolzonella & Cimatti 2019). Several competing or complementary processes are responsible for driving or ceasing the star formation in the member galaxies. The dominant processes are expected to differ across redshifts, stellar masses, halo masses, and environments (e.g. Overzier 2016). For this reason, it is still a challenge to model the red-sequence population, in particular, at high redshifts (e.g. Sommariva et al. 2014; Darvish et al. 2016; Davé, Rafeferantsoa & Thompson 2017; Chauke et al. 2019).

The redMaPPer cluster catalogues contain clusters at  $\lambda > 5$ , but the DES does not use clusters at  $5 < \lambda < 20$  for cosmology as this low richness sample is unreliable as many of the lowest richness clusters are subject to strong projection effects in the line of sight. However, these low mass samples are very interesting for astrophysical studies (e.g. Conroy & Wechsler 2009; Wechsler & Tinker 2018). By definition, these systems have few members and problems with Poisson statistical noise become important. However, even a modest shift towards lower  $\lambda$  values could potentially have a significant impact on cosmology. This is a challenging regime but the potential impact makes it worth exploring alternative mass proxies that might be more robust against projection effects. Alternative optical mass proxies are possible (Andreon 2012; Mulroy et al. 2017; Pereira et al. 2018; Bellagamba et al. 2019; Palmese et al. 2020;

Sampaio-Santos et al. 2020). For example, one could incorporate the count of star-forming galaxies into the richness. This would be of particular interest at low masses and high redshifts.

In Pereira et al. (2018) and Palmese et al. (2020), we introduced and studied a physically motivated mass proxy named  $\mu_*$ , which is based on the total stellar mass and therefore accounts for the red and blue members of the clusters. Andreon (2012) was the first to propose a stellar-mass-based mass proxy for clusters, but since then such kind of proxy has mostly been studied in simulations (Ascaso et al. 2016, 2017; Farahi et al. 2018; Kravtsov, Vikhlinin & Meshcheryakov 2018; Bradshaw et al. 2020).

In particular, Bradshaw et al. (2020) showed that a stellar mass proxy similar to  $\mu_*$  has less intrinsic scatter with halo mass than a richness proxy and is less affected by projection effects. They used a set of simulations for this comparison, in which they identify haloes and compute the intrinsic scatter in the virial mass at fixed proxy by: (i) using the true redshifts, i.e. no projection effects; (ii) simulating a spectroscopic survey with precise redshift measurements; and (iii) simulating a photometric survey with a redshift uncertainty of  $\sigma_z/(1+z) = 0.01$ . In all these cases, they showed that the proxy based in the total stellar mass presented lower intrinsic scatter than the  $\lambda$ -like proxy (see their fig. 3).

In Pereira et al. (2018), we provided a first calibration of the mass– $\mu_*$  relation at low  $z$  using the Sloan Digital Sky Survey (SDSS) Stripe 82 data. In this work, we use stacked weak-lensing signal to measure the mean galaxy cluster mass of redMaPPer clusters identified in the DES Y1 data using  $\mu_*$  as a mass proxy. For the first time, we calibrate the mass– $\mu_*$ –redshift relation of these clusters at moderate redshifts ( $z \leq 0.7$ ). We also incorporate a variety of improvements to the weak-lensing modelling and perform a blinded analysis.

This paper is organized as follows. In Section 2, we describe the cluster and the lensing shear catalogues. In Section 3, we present the methodology for the measurement and modelling of the stacked cluster masses. We present the modelling and the derived mass calibration in Sections 4 and 5, respectively. Finally, in Section 6, we present our concluding remarks and we summarize our results in Section 7.

In this paper, the distances are expressed in physical coordinates, magnitudes are in the AB system (unless otherwise noted), and we denote logarithm base 10 as  $\log$  and logarithm base  $e$  as  $\ln$ . We assume a flat Lambda cold dark matter ( $\Lambda$ CDM) cosmology with a matter density  $\Omega_m = 0.3$  and a Hubble parameter  $h = H_0/100 \text{ km s}^{-1} \text{ Mpc}^{-1} = 1$ .

## 2 THE DES Y1 CATALOGUES

The DES (The Dark Energy Survey Collaboration 2005, 2016) is an optical imaging survey that observed 5000 square deg of the celestial Southern hemisphere using the 4-m Blanco Telescope and the Dark Energy Camera (Flaugh et al. 2015) at the Cerro Tololo Inter-American Observatory (CTIO) in Chile. The main goal of the survey is to constrain the distribution of dark matter in the Universe, and the amount and properties of dark energy, including its equation of state. DES used the *grizY* bands to obtain photometric redshifts and reaching limiting magnitudes of  $i \sim 24$ . Due to the large area, depth, and image quality of DES, we expect to have an optical identification of a large number of galaxy clusters and groups ( $\sim 100\,000$ ) up to a redshift of  $z \sim 1$ .

The DES observations were carried out during roughly one semester per year, and the first full operating season took place from 2013 August to 2014 February, DES Y1 (Diehl et al. 2014; Drlica-Wagner et al. 2018). Before this, a small Science Verification

(SV) survey was conducted from 2012 November to 2013 February. The SV data covered 250 square deg, reaching almost the depth of the complete survey.

During the DES Y1 observations, 1839 square deg of the southern sky were observed in three to four tilings in the *griz* bands as well as 1800 square deg in the *Y* band. The resulting imaging is shallower than the SV data but covers a significantly larger area. In the DES Y1 we have  $\sim 1500$  square deg of the main survey, divided into two large non-contiguous areas. The reduction in the area is due to a series of survey masks. These masks are applied to avoid bright stars, satellite tracks, and the Large Magellanic Cloud, among others. The two non-contiguous areas are the ‘SPT’ area (1321 square deg), which overlaps the footprint of the 2500 square deg South Pole Telescope Sunyaev-Zel’dovich Survey (Carlstrom et al. 2011), and the ‘S82’ area (116 square deg), which overlaps the Stripe-82 deep field of the SDSS (Annis et al. 2014). In this study, we utilize data from the SPT region.

The data from the first three seasons were the basis for the first DES public data release<sup>1</sup> (Abbott et al. 2018b). The data processing for Y5 has already been completed and the final observing season, Y6, was finalized on 2019 January 9.

In the following, we briefly describe the catalogues used in this analysis and refer the reader to the corresponding papers for more details. The photometric redshift and weak-lensing shape catalogues were used in the main DES cosmological analysis combining galaxy clustering and weak lensing (Abbott et al. 2018a).

## 2.1 redMaPPer cluster catalogue

In this work, we use the ‘volume-limited’ catalogue of photometrically selected clusters identified in the DES Y1 data by the redMaPPer cluster-finding algorithm v6.4.17 (Rykoff et al. 2014, 2016). In this catalogue,<sup>2</sup> a galaxy cluster is included in the sample only if all cluster member galaxies brighter than the luminosity threshold used to define cluster richness in redMaPPer are above  $3\sigma$  limiting magnitude in *g*,  $5\sigma$  in *r* and *i*, and  $10\sigma$  in *z* according to depth maps of the survey (Drlica-Wagner et al. 2018).

As previously mentioned, redMaPPer uses multiband colours to find overdensities of red-sequence galaxies around candidate central galaxies. In the DES Y1 data, redMaPPer uses the four band magnitudes (*griz*) and their errors to spatially group the red-sequence galaxies at similar redshifts into cluster candidates. Starting from an initial set of spectroscopic seed galaxies, the algorithm iteratively fits a model for the local red sequence, and for each red galaxy, redMaPPer estimates its membership probability ( $p_{\text{mem}}$ ) following an iteratively self-trained matched-filter technique. At the end, for each identified cluster, redMaPPer returns an optical richness estimate  $\lambda$  [the sum over the membership probabilities of all red galaxies within a pre-defined, richness-dependent projected radius  $R_\lambda = (\lambda/100)^{0.2}h^{-1}\text{Mpc}$ ], a photo-*z* estimate  $z_\lambda$  (obtained by maximizing the probability that the observed colour distribution of likely members matches the self-calibrated red-sequence model of redMaPPer), the positions (RA, Dec), and a vector with the probabilities of the five most likely central galaxies ( $P_{\text{cen}}$ ).

This catalogue contains more than 76 000 clusters down to  $\lambda > 5$  and out to  $z_\lambda \sim 0.8$ , of which more than 6000 are above  $\lambda \geq 20$ . For each cluster in this catalogue, we computed the value of the mass proxy  $\mu_*$ , which will be described in the next section. In Fig. 1,

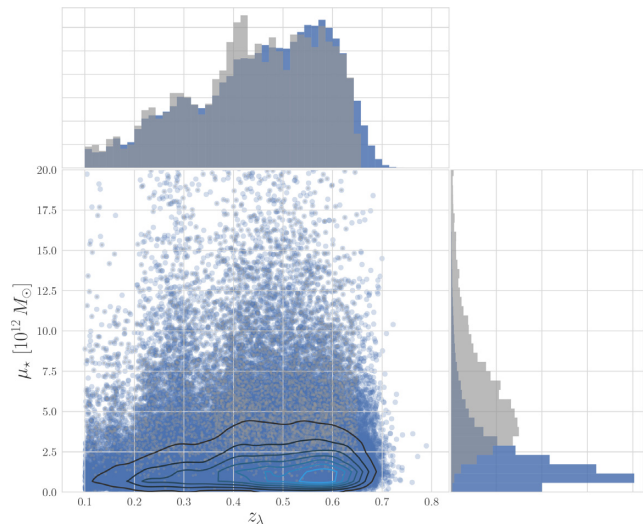


**Figure 1.** Redshift- $\mu_*$  distribution of the redMaPPer clusters in the volume-limited DES Y1 cluster catalogue with  $\lambda > 5$  (blue dots) overlaid with density contours to highlight the densest regions and the redshift- $\mu_*$  distribution of the clusters ( $\lambda > 20$ ,  $0.1 \leq z < 0.65$ ) used in this analysis (grey dots). At the top and on the right are normalized histograms of the projected quantities,  $z_\lambda$  and  $\mu_*$ , respectively, for the full catalogue (in blue) and for the subsample used in this work (in grey).

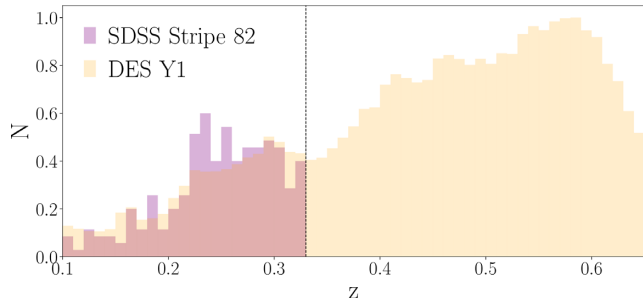


**Figure 2.** Normalized redshift distribution: 230 clusters in the SDSS Stripe 82 sample (purple) and 6124 clusters in DES Y1 sample (orange). In both histograms, the catalogue used corresponds to the  $\lambda > 20$  samples. The vertical dotted line shows the  $z$  limit ( $z = 0.33$ ) in which the previous calibration of  $\mu_*$  has been performed.

we show the cluster  $\mu_*$  and redshift distributions for the volume-limited catalogue ( $\lambda > 5$ ) in blue. Because the spectroscopic training sample goes only to  $z \sim 0.65$ , the catalogue should be robust just within this range. To avoid complications with selection functions and unreliable detections due to projection effects, in this work we just use the sample with  $\lambda > 20$ , which is the sample used in the main cosmology analysis of DES. Thus, in grey we show the cluster sample we use:  $0.1 < z < 0.65$  and  $\mu_* < 5.5 \times 10^{13} \text{ M}_\odot$  with a total of 6124 galaxy clusters.

In Pereira et al. (2018), we performed the first mass calibration of  $\mu_*$  for the SDSS Stripe 82 redMaPPer catalogue of  $\lambda > 20$  and  $0.1 < z < 0.33$  with a total of 230 clusters and using shear data from the Canada–France–Hawaii Telescope Stripe 82 Survey (CS82; Moraes et al. 2014). In Fig. 2, we show the comparison of the normalized redshift distribution of the SDSS Stripe 82 sample (purple) with the DES Y1 sample (orange) of  $\lambda > 20$  and  $0.1 < z < 0.65$ . It illustrates the increase towards higher redshifts and the statistical gain compared to the previous work, which allows us to study the

<sup>1</sup><https://www.darkenergysurvey.org/>

<sup>2</sup><https://des.ncsa.illinois.edu/releases/y1a1/key-catalogs/key-redmapper>

redshift evolution of our MOR and reduce the statistical errors in our mass measurements.

## 2.2 Photometric redshift catalogue

To estimate physical quantities such as  $\mu_*$  and the mass from the lensing signal, we need to know the redshift of the member galaxies and the source galaxies being lensed, respectively. We also need the information about the individual  $P(z)$  of source galaxies for computing the boost-factors profiles.

We use the photometric redshift catalogue<sup>3</sup> of DES Y1 produced and validated by Hoyle et al. (2018) using the template-based BPZ<sup>4</sup> algorithm (Benítez 2000; Coe et al. 2006). Hoyle et al. (2018) found that these photo- $z$  estimates were biased and needed an overall multiplicative systematic correction in the recovered weak-lensing profiles. Following McClintock et al. (2019), we determine this correction and present it in Section 3. We also use two separate BPZ catalogues: one generated from the single-epoch METACALIBRATION-measured photometry for selecting and weighting sources, and one from a multi-epoch, multiobject fitting (MOF) photometry for determining the resulting source redshift distributions.

## 2.3 Assigning $\mu_*$ for redMaPPer clusters

The  $\mu_*$  mass proxy relies on the clear physical meaning of the total stellar mass of a cluster and, in particular, Palmese et al. (2020) showed that the scatter in the  $\mu_*$ -to-X-ray temperature relation is comparable to other mass proxies (in particular, to the redMaPPer  $\lambda$ ), for an X-ray sample.

In Pereira et al. (2018) and Palmese et al. (2020), we describe in detail how the mass proxy  $\mu_*$  is computed. The assignment of  $\mu_*$  is the last step in the modular pipeline VT-CLUSTERTOOLS  that we are developing and which consists of: (i) cluster finding (optional, since any cluster catalogue can be given as input); (ii) probabilistic membership assignment; (iii) total stellar-mass measurements and  $\mu_*$  estimation.

We use DES Y1 redMaPPer catalogue as input and performed the membership assignment and stellar mass measurements. First, we compute the membership probability  $P_{\text{mem}}$  for each cluster galaxy as

$$P_{\text{mem}} = P_z P_r, \quad (1)$$

where the two components represent the probability of the galaxy to be a member given its redshift ( $P_z$ ) and its distance from the cluster centre ( $P_r$ ). In practice,  $P_z$  is the integrated photometric redshift probability distribution of each galaxy within a  $\Delta z = 0.1$  window around the cluster redshift.  $P_r$  is computed assuming a projected Navarro–Frenk–White (NFW) profile from Wright & Brainerd (2000), where  $r_{200}$  is defined as the radius at which the mass density of the cluster is 200 times greater than the critical density of the Universe  $\rho_{\text{crit}} = 3H^2(z)/8\pi G$ , where  $H(z)$  is the respective Hubble parameter. For the concentration parameter we assume a fixed value of  $c = 3$ .

After computing the membership probabilities for each galaxy  $i$  within 3 Mpc of each cluster  $j$ , we compute their stellar masses assuming that every member galaxy is at the redshift of its host,  $M_{*,i}(z_j)$ . Since the cluster redshifts have smaller uncertainties than individual galaxies' redshifts, this minimizes the uncertainties on

$M_{*,i}$  measurements. The stellar masses are computed using the code presented in Palmese et al. (2020), based on Bayesian Model Averaging (Hoeting et al. 1999). Our method takes into account the uncertainty on model selection by averaging over a robust sample of stellar population synthesis models, and by marginalizing over the model uncertainty. Similarly to Palmese et al. (2020), we generate these models using the flexible stellar population synthesis code from Conroy & Gunn (2010). The computation assumes Padova (Girardi et al. 2000, Marigo & Girardi 2007, Marigo et al. 2008) isochrones and Miles (Sánchez-Blázquez et al. 2006) stellar libraries with four different metallicities ( $Z = 0.03, 0.019, 0.0096$ , and 0.0031). We use a Salpeter initial mass function (Salpeter 1955) and the Simha et al. (2014) four-parameter star formation history (SFH):

$$\text{SFR}(t) = \begin{cases} A(t - t_i) e^{(t-t_i)/\tau} & \text{if } t < t_i \\ \text{SFR}(t_i) + \tan\theta(t - t_i) & \text{otherwise,} \end{cases} \quad (2)$$

where  $A$  is a normalization factor,  $t_i$  is the time at which star formation starts,  $\tau$  is the exponential time-scale at  $t < t_i$ , with  $t_i$  being the time of transitions from exponential to linear fall off, and  $\tan\theta$  is the slope of the SFH after  $t_i$ . In our models, we let the four model parameters vary over the following ranges:  $\tau \in [0.3, 13]$  Gyr,  $t_i \in [0.7, 2]$  Gyr,  $t_i \in [7, 13]$  Gyr, and  $\theta \in [-10, -80]$  deg.

Once the stellar masses are computed, we define the mass proxy  $\mu_*$  as the sum of the individual galaxy stellar masses weighted by their membership probability

$$\mu_* = \sum_i P_{\text{mem},i} M_{*,i}. \quad (3)$$

The membership assignment and  $\mu_*$  computation were performed in the full DES Y1 volume-limited catalogue with  $\lambda > 5$ , but throughout this work we only use the clusters with  $\lambda > 20$  to make sure that our analysis is done in the same regime as the current  $\lambda$ -sample to facilitate comparisons between the two mass proxies.

## 2.4 Weak-lensing shear catalogue

We use the shape measurements from the METACALIBRATION (Huff & Mandelbaum 2017; Sheldon & Huff 2017) shape catalogue<sup>5</sup> of DES Y1 presented in Zuntz et al. (2018). The METACALIBRATION  code utilizes images taken in the  $r/z$  bands to measure the ellipticities of the galaxies. The algorithm works by distorting the image with a small known shear and calculating the response of a shear estimator to that applied shear. In this method, there is no need for prior information about galaxy properties or a calibration from simulations. The fiducial shear estimates are obtained from a single Gaussian fit by using the NGMIX  model-fitting algorithm (Sheldon 2015). The produced DES Y1 METACALIBRATION catalogue has an effective source density of  $6.28 \text{ arcmin}^{-2}$ .

The main systematic effect in this shape estimation is a multiplicative bias, i.e. an over- or underestimation of the gravitational shear inferred from the mean tangential ellipticity of the lensed galaxies. To characterize and correct for this bias, METACALIBRATION uses the galaxy images themselves to 'de-bias' the shear estimates.

The METACALIBRATION shear catalogue and the associated calibration of the source redshift distributions (Hoyle et al. 2018) were extensively tested and validated by Zuntz et al. (2018) and Prat et al. (2018), making this lensing catalogue well tested for different applications.

<sup>3</sup><https://des.ncsa.illinois.edu/releases/y1a1/key-catalogs/key-photoz>

<sup>4</sup><http://www.stsci.edu/~dcoe/BPZ/>

<sup>5</sup><https://des.ncsa.illinois.edu/releases/y1a1/key-catalogs/key-shape>

**Table 1.** Binning scheme and properties of the DES Y1 redMaPPer cluster sample. We split the clusters into three redshift bins and choose the  $\mu_*$  bins to have a similar number of clusters in each of the four bins. Here  $\mu_*$  is in units of  $10^{12} M_\odot$ .

$z$ range	Mean $z$	$\mu_*$ range	Mean $\mu_*$	No. of clusters
[0.1, 0.33)	0.232	[0, 3.3)	2.38	318
	0.233	[3.3, 5.0)	4.10	317
	0.243	[5.0, 7.5)	6.15	313
	0.259	[7.5, 60)	12.6	402
[0.33, 0.5)	0.424	[0, 4.04)	3.06	571
	0.420	[4.04, 5.65)	4.83	567
	0.420	[5.65, 8.05)	6.73	567
	0.427	[8.05, 60)	12.98	744
[0.5, 0.65)	0.572	[0, 3.88)	2.96	554
	0.574	[3.88, 5.42)	4.67	555
	0.573	[5.42, 7.68)	6.46	556
	0.570	[7.68, 60)	11.71	660

### 3 THE STACKED CLUSTER PROFILES

We measure the mass of the DES Y1 redMaPPer clusters from their stacked weak-lensing signal using the METACALIBRATION shear catalogue and BPZ photo- $z$ 's. For the stacking of the lenses, we define bins of redshift and  $\mu_*$ . The redshift bins are defined as  $z_{\text{low}}$  ( $0.1 \leq z < 0.33$ ),  $z_{\text{mid}}$  ( $0.33 \leq z < 0.5$ ), and  $z_{\text{high}}$  ( $0.5 \leq z < 0.65$ ). To remove the few outlier cases in which the stellar-mass-fitting code generated non-physical values for one or more of the member galaxies, we apply an upper limit cut in the  $\mu_*$  range such that the clusters in these three redshift bins lie within the range  $\mu_* < 5.5 \times 10^{13} M_\odot$ . In each redshift bin, we separate the samples into four  $\mu_*$  bins, in such a way that we have a similar number of clusters in each bin. In Table 1, we summarize the binning scheme for our stacking measurements.

#### 3.1 Projected surface mass density profiles

In the weak-lensing regime, a non-linear combination of the gravitational shear  $\gamma$  and convergence  $\kappa$  defines an estimator for the 'reduced shear' (Bartelmann & Schneider 2001)

$$\mathbf{g} \equiv \frac{\gamma}{1 - \kappa}. \quad (4)$$

In practice, we assume  $\langle \mathbf{g} \rangle \approx \langle \gamma \rangle \approx \langle \mathbf{R} \rangle^{-1} \langle \mathbf{e} \rangle$ . Here  $\mathbf{R}$  is a joint response matrix computed as  $\mathbf{R} \approx \mathbf{R}_\gamma + \mathbf{R}_{\text{sel}}$ , where the terms on the right are the responses of the ellipticity measurement and the selection effects to the gravitational shear, respectively (see Sheldon & Huff 2017 and McClintock et al. 2019, for details).

The gravitational field from a foreground mass distribution induces correlations in the shapes of source galaxies, such that, on average, galaxy images are stretched and aligned tangentially to the centre of mass. Miralda-Escude (1991) found that, for any distribution of projected mass, it is possible to show that the azimuthally averaged tangential shear  $\gamma^T$  at a projected radius  $R$  from the centre of the mass distribution is given by

$$\gamma^T(R) = \frac{\Delta \Sigma}{\Sigma_{\text{crit}}} \equiv \frac{\overline{\Sigma}(< R) - \overline{\Sigma}(R)}{\Sigma_{\text{crit}}}, \quad (5)$$

where  $\Sigma(R)$  is the projected surface mass density at radius  $R$ ,  $\overline{\Sigma}(< R)$  is the mean value of  $\Sigma$  within a disc of radius  $R$  given by

$$\overline{\Sigma}(< R) = \frac{2}{R^2} \int_0^R dR' R' \overline{\Sigma}(R'), \quad (6)$$

and  $\overline{\Sigma}(R)$  is the azimuthally averaged  $\Sigma(R)$  within a ring of radius  $R$  computed as

$$\overline{\Sigma}(R) = \int_{-\infty}^{+\infty} d\chi \Delta\rho \left( \sqrt{R^2 + \chi^2} \right), \quad (7)$$

where  $\chi$  is the separation along the line of sight and  $\Delta\rho$  is an average excess of a given three-dimensional matter density. Finally,  $\Sigma_{\text{crit}}$  is the critical surface mass density expressed in physical coordinates as

$$\Sigma_{\text{crit}} = \frac{c^2 D_s}{4\pi G D_l D_{ls}}, \quad (8)$$

where  $D_l$  and  $D_s$  are angular diameter distances from the observer to the lens and to the source, respectively, and  $D_{ls}$  is the angular diameter distance between lens and source.

To perform precise measurements of the surface density contrast  $\Delta\Sigma$ , we need to estimate the redshifts of the lens (i.e. galaxy clusters) and the source galaxies robustly. We use the photometric redshift estimates from the redMaPPer algorithm as the lens redshifts. Due to a negligible statistical uncertainty on these estimates ( $\Delta z_l \approx 0.01$ ; Rykoff et al. 2016), compared to other sources of error in the lensing measurement, we can treat these redshifts as exact. The redshift of source galaxies is also photometric, and is described by a probability distribution  $p_{\text{phot}}(z_s)$  for each source galaxy. Thus, we estimate an effective critical surface density as

$$\langle \Sigma_{\text{crit}}^{-1} \rangle_{j,i} = \int dz_{s,i} p_{\text{phot}}(z_{s,i}) \Sigma_{\text{crit}}^{-1}(z_{s,i}, z_{l,j}), \quad (9)$$

where  $i$  is the source and  $j$  is the lens index in a lens–source pair. We note that here we express the *inverse* critical surface density, which is in practice the amplitude of the lensing signal (see equation 5). This quantity is consistently defined as zero if  $z_s \leq z_l$ . To speed up the calculations, equation (9) is performed via Monte Carlo integration where each source at that radial range contributes with a single Monte Carlo-draw redshift value drawn from its own  $p_{\text{phot}}(z_s)$ .

From equation (5), we can compute  $\Delta\Sigma$  over several lenses with similar physical properties (e.g. redshift and stellar mass) to increase the signal-to-noise and average over the effect of substructures, uncorrelated structures in the line of sight, shape noise, and variations in the shape of individual haloes. However, in practice, using the shear and selection responses ( $\mathbf{R}_\gamma$  and  $\mathbf{R}_{\text{sel}}$ , respectively) provided in METACALIBRATION's catalogue we define a minimum variance estimator for the weak-lensing signal as

$$\widetilde{\Delta\Sigma} \equiv \frac{\sum_{j,i} \omega_{i,j} e_{T,i,j}}{\sum_{j,i} \omega_{i,j} \Sigma_{\text{crit};i,j}^{\prime-1} \mathbf{R}_{\gamma,i}^T + \left( \sum_{j,i} \omega_{i,j} \Sigma_{\text{crit};i,j}^{\prime-1} \right) \langle \mathbf{R}_{\text{sel}}^T \rangle}, \quad (10)$$

where the summation goes over all source–lens pair in a given radial bin and  $e_{T,i,j}$  is the tangential component of source  $i$  relative to the lens  $j$ . The quantities  $\mathbf{R}_{\gamma,i}^T$  and  $\langle \mathbf{R}_{\text{sel}}^T \rangle$  are proportional to the trace of the shear and selection response matrices, respectively, and their detailed definitions can be found in Zuntz et al. (2018) and McClintock et al. (2019), but it is important to note that these selection responses were defined by the photometric redshift estimates derived from the sheared METACALIBRATION photometry.

To speed up the computation of equation (10), we use two simplifications: (i) replace the expectation value of the normalization  $\Sigma_{\text{crit}}^{\prime-1}$  by a Monte Carlo estimate

$$\Sigma_{\text{crit};i,j}^{\prime-1} = \Sigma_{\text{crit}}^{\prime-1}(z_{l,j}, z_{s,i}^{\text{MC}}), \quad (11)$$

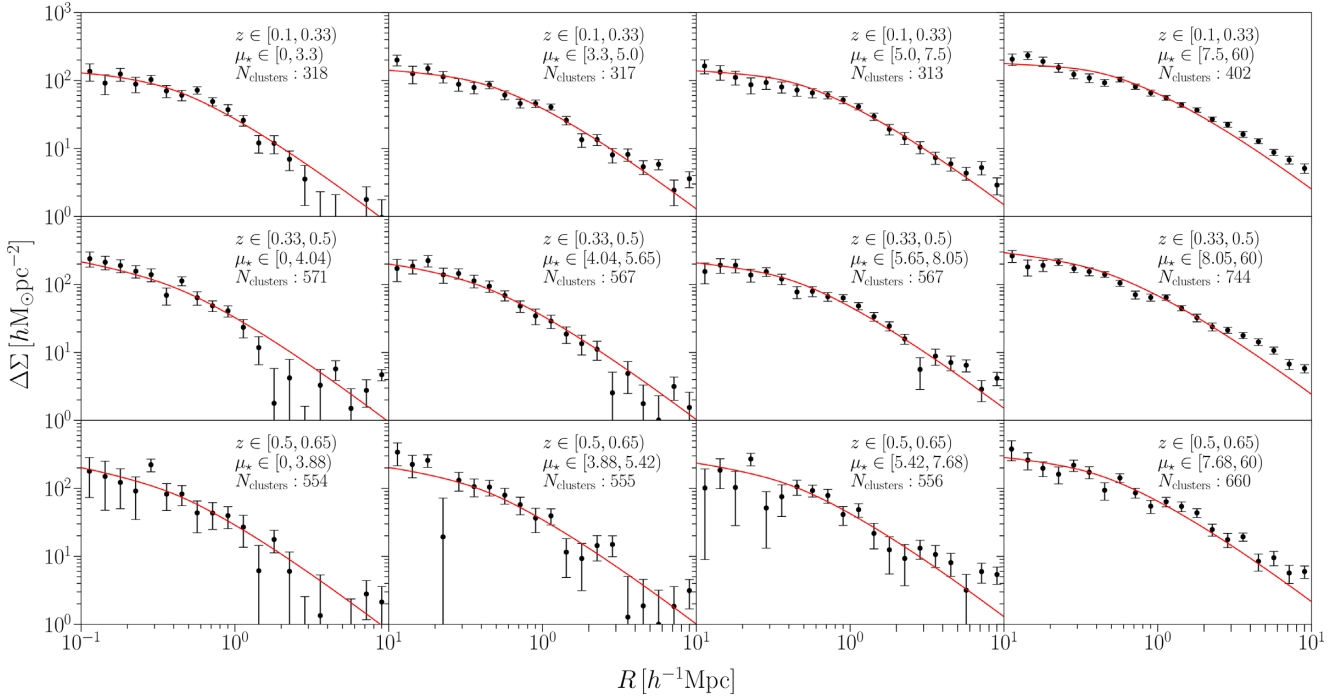


**Figure 3.** The mean  $\Delta\Sigma$  for cluster subsets separated in  $z_l$  (increasing from *top* to *bottom*) and  $\mu_\star$  (increasing from *left* to *right*) with errors from jackknife resampling (see Section 3.2). The best-fitting model (red curve) includes the corrections in equation (32); see Section 3 for details. In the legend,  $\mu_\star$  is in units of  $10^{12} M_\odot$ .

where  $z_{s_i}^{\text{MC}}$  is a random sample from the  $p_{\text{phot}}(z_s)$  distribution estimated with BPZ using MOF photometry; (ii) choose the weights as

$$\omega_{i,j} \equiv \Sigma_{\text{crit}}^{-1}(z_{l_j}, \langle z_{s_i}^{\text{MCAL}} \rangle) \text{ if } \langle z_{s_i}^{\text{MCAL}} \rangle > z_{l_j} + \Delta z, \quad (12)$$

where  $\langle z_{s_i}^{\text{MCAL}} \rangle$  is the mean redshift of the source galaxy estimated from METACALIBRATION photometry. We use separation of  $\Delta_z = 0.1$  from the lens redshift for source selection. McClintock et al. (2019) found that including the source weights provided by METACALIBRATION does not introduce a significant improvement in the signal-to-noise of the measurement. They also argue that the use of two different photometric estimators is necessary because when calculating the selection response, the internal photometry of the METACALIBRATION must be used for all selections and weightings of sources.

In addition to that, Hoyle et al. (2018) found that photo- $z$  estimates from METACALIBRATION have a greater scatter than the ones estimated with MOF photometry. Therefore, we follow the approach of McClintock et al. (2019) expressed in equation (10), where we use the METACALIBRATION photo- $z$  estimates for selecting and weighting the source–lens pairs and we use the MOF-based photo- $z$  estimates for computing the normalization of the shear signal to find  $\Delta\Sigma$ .

To estimate the weak-lensing signal  $\Delta\Sigma$  from equation (10), we use a modified version of the XSHARP [code](#) implemented in the XPIPE [PYTHON](#) package. The clusters are grouped into three bins in redshift:  $z \in [0.1, 0.33]$ ,  $[0.33, 0.5]$ , and  $[0.5, 0.65]$ , as well as four bins in  $\mu_\star$  as described in Table 1. We measure the  $\Delta\Sigma$  profiles in 20 logarithmic radial bins in the range  $(0.1-10) h^{-1} \text{ Mpc}$ . The measured  $\Delta\Sigma$  profiles are shown in Fig. 3. We computed the cross-component of the lensing signal ( $\Delta\Sigma_x$ ) and found no evidence of spurious correlations in the weak-lensing signals, i.e. the measured  $\Delta\Sigma_x$  are consistent with zero. McClintock et al. (2019) described a series of tests and validation for systematics of the source catalogue

such as shear and photometric redshift bias and cluster-members contamination. Since we rely on the same catalogue, the treatment of this systematics could be applied to our work and is described in detail in the next sections.

### 3.2 Covariance matrices for $\Delta\Sigma$

In Pereira et al. (2018), the measurements were shape-noise dominated such that the covariance between adjacent radial bins was not noticeable and the  $\Delta\Sigma$  measurements in each bin were treated as independent. However, for the DES Y1 sample, this assumption does not hold anymore. Besides the shape noise, the uncertainty in the  $\Delta\Sigma$  measurements has contributions from the uncertainty in the photometric redshift estimations, and the intrinsic variations of cluster profiles. Furthermore, in a stacked cluster lensing analysis in a given survey area, source galaxies are paired with multiple clusters, possibly generating covariance between different radial bins as well as different cluster bins in  $\mu_\star$  and redshift. Therefore, the cluster  $\Delta\Sigma$  measurements are not fully independent, and we need to estimate the covariance matrix  $\mathbf{C}_{\widetilde{\Delta\Sigma}}$  that will have significant off-diagonal terms, in particular, on large scales.

Following McClintock et al. (2019), to estimate  $\mathbf{C}_{\widetilde{\Delta\Sigma}}$  we use a spatial jackknife (JK) scheme designed to account for the covariance of the measurements. We use a JK resampling with  $K = 100$  simply connected spatial regions  $R_k$  selected by running a K-MEANS [algorithm](#) on the sphere. The JK covariance is defined as in Efron (1982) by

$$\mathbf{C}_{\widetilde{\Delta\Sigma}} = \frac{K-1}{K} \sum_k^K \left( \widetilde{\Delta\Sigma}_{(k)} - \widetilde{\Delta\Sigma}_{(.)} \right)^T \cdot \left( \widetilde{\Delta\Sigma}_{(k)} - \widetilde{\Delta\Sigma}_{(.)} \right), \quad (13)$$

where  $\widetilde{\Delta\Sigma}_{(.)} = \frac{1}{K} \sum_k \widetilde{\Delta\Sigma}_{(k)}$ , and  $\widetilde{\Delta\Sigma}_{(k)}$  is the lensing signal estimated through equation (10), using all lenses except those in the

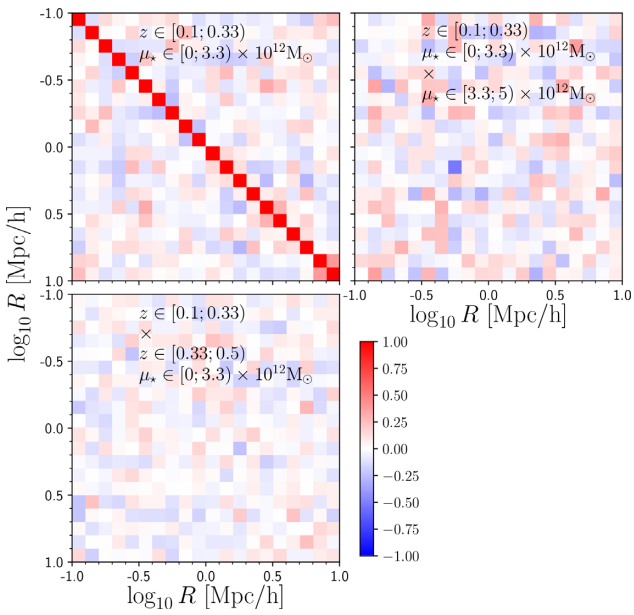


**Figure 4.** Correlation matrix of  $\Delta\Sigma$  of a single profile with  $z \in [0.1, 0.33]$  and  $\mu_* \in [0; 3.3) \times 10^{12} M_\odot$ , estimated from 100 jackknife regions (upper left panel). The off-diagonal blocks show the correlation matrix between the reference profile and the neighbouring bin,  $\mu_* \in [3.3; 5.0) \times 10^{12} M_\odot$  (upper right panel), and the neighbouring redshift bin  $z \in [0.33, 0.5)$  (lower left panel).

region  $R_k$ . In Fig. 4, we present an example of the estimated JK correlation matrix for the bin  $z \in [0.1, 0.33]$  and  $\mu_* \in [0, 3.3) \times 10^{12} M_\odot$ . We can see that on smaller scales the diagonal is dominant, but off-diagonal terms are present for the largest scales, as expected. We check the cross-correlations between the profiles measured in different  $z$  and  $\mu_*$  subsets, and find them to be small (cf. upper right and lower left panel of Fig. 4). Therefore, we will assume no cross-correlation between different cluster subsets in our likelihood for fitting  $\Delta\Sigma$ .

### 3.3 Projected surface mass density model

To infer the average masses from the weak-lensing signal around each lens, we use a two-components model given by a perfectly centred dark matter halo profile and an offset profile where the assumed centre does not correspond to the dynamical centre of the dark matter halo ('*miscentring term*'), such that our  $\Delta\Sigma$  model is given by

$$\Delta\Sigma_{\text{model}} = p_{\text{cc}}\Delta\Sigma_{\text{cen}} + (1 - p_{\text{cc}})\Delta\Sigma_{\text{misc}}, \quad (14)$$

where  $p_{\text{cc}}$  is the fraction of correctly centred clusters. For the centred profile, we could also consider the contribution of neighbouring haloes through the 'two-halo' term for the outer regions of the halo. However, for computational reasons, we choose to apply a radial cut ( $R < 2.5$  Mpc) while performing the profile fitting of  $\Delta\Sigma$  to minimize the effects of the two-halo term. We have tested in simulations that this approach has negligible effects in the amplitude of the recovered  $\Delta\Sigma$  (i.e. changes of 1–3 per cent).

We model the centred term as a NFW (Navarro, Frenk & White 1996) three-dimensional density profile given by

$$\rho(r) = \frac{\delta_c \rho_{\text{crit}}}{\frac{r}{r_s} \left(1 + \frac{r}{r_s}\right)^2}, \quad (15)$$

where  $r_s$  is the cluster scale radius,  $\delta_c$  is the characteristic halo overdensity, and  $\rho_{\text{crit}}$  is the critical density of the Universe at the lens redshift.

In this paper, we use the mass  $M_{200}$  contained within a radius  $r_{200}$  where the mean mass density is 200 times the critical density of the Universe. The scale radius is given by  $r_s = r_{200}/c_{200}$ , where  $c_{200}$  is the concentration parameter. In our fitting procedure, we fix  $c_{200}$  by assuming the semi-analytic concentration model of Diemer & Joyce (2019) available in the COLOSSUS (Diemer 2015) PYTHON package.

Bartelmann (1996) and Wright & Brainerd (2000) provide an analytical expression for the projected NFW profile,  $\Delta\Sigma_{\text{NFW}}$ , and we use the PYTHON code NFW (Dietrich 2016) that implements these results for our profile-fitting procedure. Thus, the centred term in equation (14) is given by this  $\Delta\Sigma_{\text{NFW}}$ . In the next section, we describe our model for the miscentring term, i.e. the  $\Delta\Sigma_{\text{misc}}$  for NFW density profiles.

#### 3.3.1 Miscentring modelling

Miscentring can be caused by a simple failure in the centre assignment by the cluster finder algorithm. Also, many cluster finders assume as centre the position of the *brightest cluster galaxy* (BCG). Zitrin et al. (2012) show that some BCGs present an offset from the centre of their host dark matter halo. This offset was also studied in simulations (Kim, Peter & Wittman 2017; Harvey et al. 2019). The redMaPPer code does not assume, necessarily, the position of the BCG as the cluster centre. Instead, redMaPPer uses a probabilistic approach to identify the top five most likely central candidates. Thus, the cluster position is given by the highest likelihood central galaxy. However, Rykoff et al. (2016) found that  $\sim 80$ –85 per cent of the redMaPPer central galaxies are BCGs and then subject to miscentring. In fact, Zhang et al. (2019a) using high-quality X-ray data found that  $75 \pm 8$  per cent of redMaPPer clusters are well centred. The miscentring affects the observed shear profile (Yang et al. 2006; Johnston et al. 2007; Ford et al. 2014) and should be corrected. Therefore, we should estimate the miscentred differential mass density profiles as

$$\Delta\Sigma_{\text{misc}}(R) = \bar{\Sigma}_{\text{misc}}(< R) - \bar{\Sigma}_{\text{misc}}(R). \quad (16)$$

We follow the modelling scheme presented in Johnston et al. (2007), George et al. (2012), Ford et al. (2015), Simet et al. (2017), and Pereira et al. (2018) to compute the terms in equation (16). For a two-dimensional offset in the lens plane  $R_s$ , the azimuthal average of the profile is

$$\bar{\Sigma}_{\text{misc}}(R) = \int_0^\infty dR_s P(R_s) \Sigma(R|R_s), \quad (17)$$

where

$$\Sigma(R|R_s) = \frac{1}{2\pi} \int_0^{2\pi} d\theta \Sigma \left( \sqrt{R^2 + R_s^2 + 2RR_s \cos\theta} \right). \quad (18)$$

That is, the angular integral of the profile  $\Sigma(R)$  is shifted by  $R_s$  from the centre. The probability distribution of  $R_s$  is given by

$$P(R_s) = \frac{R_s}{\sigma_{\text{off}}^2} \exp \left( -\frac{1}{2} \frac{R_s^2}{\sigma_{\text{off}}^2} \right), \quad (19)$$

which is an *ansatz* assuming that the mismatching between the centre and  $R_s$  follows a Rayleigh distribution. The mean surface density inside the radius  $R$  is

$$\bar{\Sigma}_{\text{misc}}(< R) = \frac{2}{R^2} \int_0^R dR' R' \bar{\Sigma}_{\text{misc}}(R'). \quad (20)$$

We use the PYTHON code CLUSTER-LENSING  (Ford 2016; Ford & VanderPlas 2016) that implements the equations (15)–(19) to compute the miscentring term  $\Delta\Sigma_{\text{mis}}(R)$  for NFW profiles. For this miscentring profile, we only have one free parameter, the width of the offset distribution  $\sigma_{\text{off}}$ . Together with the parameter  $p_{\text{cc}}$  in equation (14), i.e. the fraction of correctly centred clusters, we would have two free parameters in our miscentring modelling.

We decided to fix  $\sigma_{\text{off}}$  with the typical value derived by Zhang et al. (2019a) for the DES Y1 redMaPPer clusters. In that work, they use a Gaussian instead of a Rayleigh distribution to model the distribution of offsets. However, our miscentring parameter  $\sigma_{\text{off}}$  is connected to their parameter  $\tau$  as

$$\sigma_{\text{off}} = \tau \times R_\lambda. \quad (21)$$

Zhang et al. (2019a) found that  $\tau = 0.17$  and in our sample, the average value of  $R_\lambda$  is  $0.78 h^{-1} \text{Mpc}$ . Therefore, we fix  $\sigma_{\text{off}} = 0.133 h^{-1} \text{Mpc}$  and keep  $p_{\text{cc}}$  as a free parameter when performing the profile fitting.

### 3.3.2 Boost-factor model

The lensing signal can be diluted due to errors in the photometric redshift estimates that can cause some of our background sources to be either in the foreground ( $z_s < z_l$ ) or to be physically associated with the lens ( $z_s = z_l$ ). To alleviate this effect, we can try to exclude all galaxies that are likely cluster members from the shape catalogue. However, due to intrinsic imperfections in the cuts, some of these galaxies leak into the source catalogue used in the weak-lensing measurement. Since foreground and physically associated galaxies are unlensed, the inclusion of these galaxies will cause  $\Delta\Sigma$  to be underestimated (the dilution effect). Therefore, the  $\Delta\Sigma$  measurements must be boosted to recover the true lensing signal, the so-called *boost-factor* correction (Kneib et al. 2003; Sheldon et al. 2004; Applegate et al. 2014; Hoekstra et al. 2015; Leauthaud et al. 2017; Melchior et al. 2017; Simet et al. 2017; McClintock et al. 2019; Varga et al. 2019).

We determine the boost-factor correction by following Gruen & Brimiouille (2017), Melchior et al. (2017), McClintock et al. (2019), and Varga et al. (2019), who make use of the estimated  $p(z)$  of the source galaxy sample to calculate the cluster contamination fraction  $f_{\text{cl}}$  and the corresponding covariance matrix  $C_{\text{fcl}}$  estimated from jackknife resampling. Then,  $f_{\text{cl}}$  is used to recover the lensing profile corrected from contamination as

$$\widetilde{\Delta\Sigma}_{\text{corr}}(R) = \frac{\widetilde{\Delta\Sigma}(R)}{1 - f_{\text{cl}}(R)}. \quad (22)$$

The  $p(z)$  decomposition method for obtaining the boost factor  $f_{\text{cl}}$  is described in detail and validated on simulated DES-like mock catalogues in Varga et al. (2019). In Fig. 5, we show an example of the measured boost-factor profile for the stack with  $z \in [0.1, 0.33]$  and  $\mu_* \in [0; 3.3] \times 10^{12} M_\odot$ .

Following McClintock et al. (2019), we do not apply equation (22) directly to our data but instead we dilute the amplitude of our model for the predicted profiles. By parametrizing the boost factor as  $B \equiv (1 - f_{\text{cl}})^{-1}$ , we model the cluster-member contamination by a NFW-like profile, with two free parameters ( $B_0$  and  $R_s$ ), in the form

$$B(R) = 1 + B_0 \frac{1 - F(x)}{x^2 - 1}, \quad (23)$$

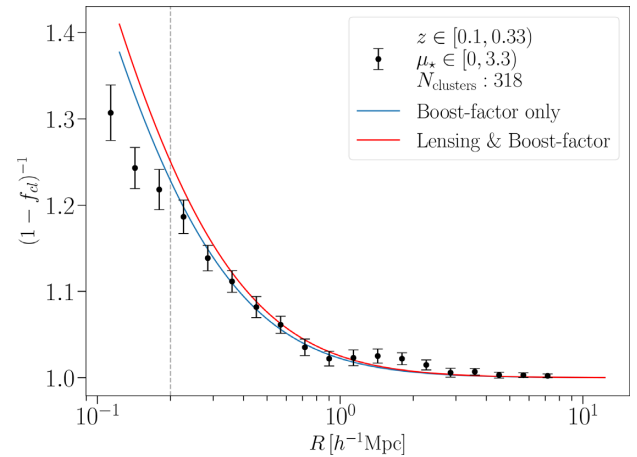


**Figure 5.** Boost-factor measurement of a single profile with  $z \in [0.1, 0.33]$  and  $\mu_* \in [0; 3.3] \times 10^{12} M_\odot$  (black dots). The blue curve is the best fit for fitting the boost-factor data alone and the red curve is the best fit for the joint fit of the lensing and boost-factor data as described in Section 3.4. The vertical dashed line shows the inner radial limit in which we performed our boost-factor fits.

where  $x = R/R_s$ , and

$$F(x) = \begin{cases} \frac{\tan^{-1} \sqrt{x^2 - 1}}{\sqrt{x^2 - 1}} & : x > 1 \\ 1 & : x = 1 \\ \frac{\tanh^{-1} \sqrt{1-x^2}}{\sqrt{1-x^2}} & : x < 1 \end{cases}. \quad (24)$$

The implementation of this model is available in the PYTHON library CLUSTER\_TOOKIT .

For each stack, we fit the measured boost factors along with the respective lensing profile, which introduces two additional parameters in our  $\Delta\Sigma$  model, namely the normalization  $B_0$  and the scaling radius  $R_s$ . When performing this joint fit of the lensing and boost-factor profiles, we try to follow McClintock et al. (2019) and use their flat priors for the boost-factor parameters. However, this choice leads to ‘unrealistic’ values for  $B_0$  and  $R_s$ . For instance, we expect a small value for the scaling radius ( $R_s < 1 h^{-1} \text{Mpc}$ ), since we have a peak in the contamination fraction at low radii (see section 4.1 of Varga et al. 2019). However, in the joint fit, we find large values for  $R_s$ , dominated by the upper limits of our priors. McClintock et al. (2019) also have shown that  $B_0$  and  $R_s$  are highly degenerate (see their fig. 10), and this might have an impact on our ability to constrain these parameters when performing the joint fit with lensing using flat priors. Therefore, we decide to perform a separated fit of the boost-factor profiles alone and use the derived values for the parameters (see Table 2) as input in a Gaussian prior when performing the joint fit with the lensing profiles (see Section 3.4).

### 3.3.3 Reduced shear

In practice, we measure the reduced shear  $\mathbf{g}$  instead of the true shear  $\gamma$  (see equation (4)). To account for this approximation, we multiply our  $\Delta\Sigma$  model by the factor

$$G(R) = \frac{1}{1 - \kappa} = \frac{1}{1 - \Sigma(R)\Sigma_{\text{crit}}^{-1}}, \quad (25)$$

where  $\Sigma_{\text{crit}}^{-1}$  is defined in equation (8) and  $\Sigma(R)$  is

$$\Sigma(R) = p_{\text{cc}}\Sigma_{\text{cen}} + (1 - p_{\text{cc}})\Sigma_{\text{mis}}, \quad (26)$$

**Table 2.** Best-fitting parameters from fitting the boost factors without the lensing profiles. We use the following flat priors:  $R_s = [0, 10]$  and  $B_0 = [0, 1]$ .

$\mu_{\star} [10^{12} M_{\odot}]$	$z$	$B_0$	$R_s [\text{Mpc}]$
[0.0, 3.3)	[0.1, 0.33)	$0.57 \pm 0.23$	$0.19 \pm 0.06$
[3.3, 5.0)		$0.26 \pm 0.12$	$0.46 \pm 0.21$
[5.0, 7.5)		$0.30 \pm 0.10$	$0.49 \pm 0.15$
[7.5, 60.0)		$0.20 \pm 0.03$	$1.01 \pm 0.17$
[0.0, 4.04)	[0.33, 0.5)	$0.23 \pm 0.34$	$0.01 \pm 0.03$
[0.04, 5.65)		$0.22 \pm 0.26$	$0.14 \pm 0.11$
[5.65, 8.05)		$0.15 \pm 0.10$	$0.23 \pm 0.09$
[8.05, 60.0)		$0.07 \pm 0.02$	$0.84 \pm 0.24$
[0.0, 3.88)	[0.5, 0.65)	$0.22 \pm 0.34$	$0.02 \pm 0.03$
[3.88, 5.42)		$0.23 \pm 0.34$	$0.13 \pm 0.34$
[5.42, 7.68)		$0.08 \pm 0.23$	$0.34 \pm 0.65$
[7.68, 60.0)		$0.29 \pm 0.26$	$0.16 \pm 0.09$

where  $\Sigma_{\text{cen}}$  comes from equation (7) and  $\Sigma_{\text{mis}}$  from equation (17). However, this correction is expected to have a negligible effect in our results.

### 3.3.4 Shear and photo- $z$ bias

In the weak-lensing analysis, two major sources of systematics are the shape measurements and photo- $z$  uncertainties. The former can lead to wrong shear estimates and the latter can bias the distance measurements leading to a biased  $\Sigma_{\text{crit}}$ , consequently affecting our  $\Delta\Sigma$  estimates. Zuntz et al. (2018) have tested for several sources of bias in the shear measurements; in particular, self-calibration of the images allowed them to determine the multiplicative  $m$  and the additive  $c$  biases. They found no evidence of a significant additive bias term but estimated the multiplicative bias to be  $m = 0.012 \pm 0.013$ .

Hoyle et al. (2018) and McClintock et al. (2019) present a method to calibrate the photo- $z$  estimates with precise measurements from COSMOS bands to determine the bias and its uncertainties. Briefly, they match the DES lensing source galaxies and the COSMOS galaxies according to their flux in each band and their intrinsic size. Following the same selection and weight as in Section 3.1, we compute the true weighted mean  $\Sigma_{\text{crit,TRUE}}^{\prime-1}$  from the matched COSMOS sample. The MOF  $griz$  BPZ redshift distribution samples provide a mean  $\Sigma_{\text{crit,MEAS}}^{\prime-1}$  that connects the weighted mean tangential shear to the  $\Delta\Sigma$  profile. Since the source selection for these measurements depends on the lens redshift, we need to repeat them in the cluster redshift range sampled in our analysis  $z_1 = 0.1\text{--}0.65$ .

Following McClintock et al. (2019), the model for the bias takes into account four sources of uncertainty in the calibration of photometric redshift distributions: (i) cosmic variance; (ii) photometric zero-point offsets; (iii) morphology matching; (iv) systematic uncertainty of the matching algorithm, and it is given by

$$\frac{\Sigma_{\text{crit,MEAS}}'^{-1}}{\Sigma_{\text{crit,TRUE}}'^{-1}} \equiv 1 + \delta, \quad (27)$$

where the quantity  $\delta$  is the offset between the true mean inverse critical surface density from COSMOS and  $\Sigma_{\text{crit}}^{-1}$  from our photo- $z$  estimates. We show in Fig. 6 the dependence of this ratio on lens redshift in the range of our analysis.

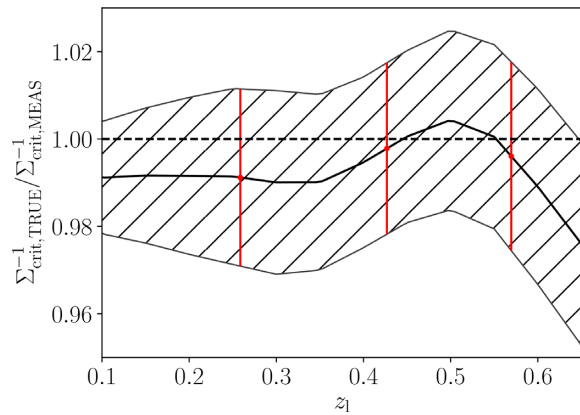


**Figure 6.** The photo- $z$  correction factor to  $\Sigma_{\text{crit}}^{-1}$  as described in Section 3.3.4. The grey hatched region indicates the  $1\sigma$  range of the correction factor. Red points with error bars show the correction factors applied in each redshift bin.

We incorporate  $\delta$  in our analysis as a prior that varies between each stack. The variations across the cluster redshift bins are

$$\delta = \begin{cases} 0.009 \pm 0.021 & \text{for } z \in [0.1, 0.33) \\ 0.002 \pm 0.020 & \text{for } z \in [0.33, 0.5) \\ 0.004 \pm 0.022 & \text{for } z \in [0.5, 0.65). \end{cases} \quad (28)$$

We combine the shear and photo- $z$  bias ( $m$  and  $\delta$ ) to define the factor  $A_m = 1 + m + \delta$ , which is included in the final likelihood as the prior

$$A_m = \begin{cases} 1.021 \pm 0.024 & \text{for } z \in [0.1, 0.33) \\ 1.014 \pm 0.024 & \text{for } z \in [0.33, 0.5) \\ 1.016 \pm 0.025 & \text{for } z \in [0.5, 0.65). \end{cases} \quad (29)$$

### 3.3.5 Triaxiality and projection effects

Cluster finders that rely on photometric data to identify galaxy clusters typically select systems that are aligned along the line of sight with higher probability. The photometric cluster selection can also be affected by the presence of other objects along the line of sight. We refer to these two effects as *triaxiality* and *projection effects*, which both affect the measured cluster MOR (White et al. 2011; Angulo et al. 2012; Noh & Cohn 2012; Dietrich et al. 2014).

Melchior et al. (2017) determined the projection effect correction factor by modelling the ratio between the average cluster stack mass not affected by projections  $\langle M \rangle_0$  and the average mass  $\langle M \rangle$  of the cluster affected by projections. They model the projected cluster as a sum of a primary halo that must have at least a mass of  $0.5\langle M \rangle_0$  and an excess mass of  $\epsilon\langle M \rangle_0$ , where  $\epsilon \in [0.0, 0.5]$ . Then, for a fraction  $p$  of clusters affected by projections, they write the average mass of the cluster stack as

$$\langle M \rangle = (1 - p)\langle M \rangle_0 + p(0.5 + \epsilon)\langle M \rangle_0. \quad (30)$$

To recover the mass in the absence of projections, i.e.  $\langle M \rangle_0$ , we should multiply the recovered weak-lensing masses by

$$\frac{\langle M \rangle_0}{\langle M \rangle} = \frac{1}{1 + p(\epsilon - 0.5)} = 1.02 \pm 0.02, \quad (31)$$

where the numerical value above was estimated from  $10^4$  Monte Carlo realizations of  $p$  and  $\epsilon$ . They adopted a Gaussian prior for  $\epsilon$  of  $\epsilon = 0.25 \pm 0.15$  such that  $\epsilon = 0$  and  $0.5$  are within  $2\sigma$  of the central value, and  $p = 10 \pm 4$  per cent as estimated from Simet et al.

(2017). In our analysis, we are using the same clusters as McClintock et al. (2019), i.e. a richness-selected sample; therefore, we believe that it is reasonable to apply the same correction for the projection effects.

Using simulation of richness-selected clusters, Dietrich et al. (2014) estimated that triaxiality can overestimate cluster masses by  $4.5 \pm 1.5$  per cent. Melchior et al. (2017) argued that this estimate can be understood as correlated scatter between richness and weak-lensing masses leading weak-lensing masses to overestimate cluster masses by an amount of  $\exp(-\beta r \sigma_{\ln M|\lambda} \sigma_{\ln M|M_{WL}})$ , where  $\beta$  is the slope of the halo mass function,  $r$  is the correlation coefficient between richness and weak-lensing mass, and  $\sigma$ 's are the intrinsic scatters in the correspondent scaling relations. Melchior et al. (2017) adopted  $r \in [0, 0.5]$  (Noh & Cohn 2012),  $\sigma_{\ln M|\lambda} = 0.25 \pm 0.05$  (Rozo & Rykoff 2014),  $\sigma_{\ln M|M_{WL}} = 0.25 \pm 0.05$ , and  $\beta \sim 3$  to arrive at a correction factor of  $0.96 \pm 0.02$ . Palmese et al. (2020) found that  $\sigma_{\ln M|\mu_\star} = 0.26^{+0.15}_{-0.10}$ , then we could argue that we would arrive at a similar correction factor for triaxiality as in Melchior et al. (2017) for our  $\mu_\star$  sample.

Therefore, we follow Melchior et al. (2017) and McClintock et al. (2019) and apply their corrections to triaxiality and projection effects. For triaxiality, we use a multiplicative factor given by the Gaussian  $G(0.96, 0.02)$  and for projection effects a factor  $G(1.02, 0.02)$ . In both cases, we use a random draw to determine the multiplicative factors to be applied in the masses together with the model bias correction, which will be described in Section 3.5.

While this analysis was in internal review by the collaboration, the cluster cosmology results from DES Y1 were released (DES Collaboration 2020) and they found that the  $\sigma_8 - \Omega_m$  posteriors are in  $2.4\sigma$  tension with DES Y1  $3 \times 2$ pt analysis, and in  $5.6\sigma$  with Planck CMB results. They argue that this tension is most likely driven by systematics in the weak-lensing mass calibration that were not fully modelled. Currently, photometric redshifts together with triaxiality and projection effects are the systematics with the largest contributions to the error budget in the mass calibration with richness (McClintock et al. 2019). However, none of these systematics alone were found to explain the tension in the DES Y1 cluster cosmology result. However, it was shown that the proposed projections and triaxiality corrections applied in Melchior et al. (2017) and McClintock et al. (2019) are probably not enough (see fig. 12 in DES Collaboration 2020) for our current measurements, in particular, for clusters with  $\lambda \in (20, 30]$ . Therefore, we need to improve our understanding of the low-richness cluster sample to find a better model for projections and triaxiality, both in a mass-richness and in a mass- $\mu_\star$  calibration analysis. Since this is beyond the scope of this paper, then, we present our results with the corrections described in this section, acknowledging that we may not be fully accounting for the projection and triaxiality effects in our mass estimates.

### 3.4 The full model

The multiplicative corrections described in the previous sections are combined with our full model of the weak-lensing profile in the form

$$\Delta\Sigma = \frac{A_m G(R)}{B(r)} [p_{cc} \Delta\Sigma_{NFW} + (1 - p_{cc}) \Delta\Sigma_{\text{misc}}]. \quad (32)$$

This model includes the multiplicative bias  $A_m$ , the boost factor  $B(r)$ , the reduced shear correction  $G(R)$ , and the miscentring parameter  $p_{cc}$ . The log-likelihood of the  $k$ th  $\Delta\Sigma$  profile is

$$\ln L(\Delta\Sigma_k | M_k, p_{cc}, A_m, B_0, R_s) \propto -\frac{1}{2} \mathbf{D}_k^T \mathbf{C}_{\Delta\Sigma}^{-1} \mathbf{D}_k, \quad (33)$$

**Table 3.** Parameters in the lensing likelihood  $L(\Delta\Sigma)$  (equation 33) and boost-factor likelihood  $L(B)$  (equation 34). Flat priors are specified with limits in square brackets, and Gaussian priors with means  $\pm$  standard deviations.

Parameter	Description	Prior
$M_{200c}$	Halo mass	$[10^{11}, 10^{18}]$
$p_{cc}$	Correctly centred fraction	$0.75 \pm 0.08$
$A_m$	Shape and photo- $z$ bias	equation (29)
$B_0$	Boost magnitude	Table 2
$R_s$	Boost-factor scale radius	Table 2

where  $\mathbf{D} = (\widetilde{\Delta\Sigma} - \Delta\Sigma)_k$  with  $\widetilde{\Delta\Sigma}$  computed from equation (10) and  $\mathbf{C}_{\Delta\Sigma}$  is the jackknife covariance matrix of  $\Delta\Sigma$ . The corresponding log-likelihood of the measured  $f_{\text{cl},k}$  in the  $k$ th cluster subset given the parameters in equation (23) is

$$\ln L(f_{\text{cl},k} | B_0, R_s) \propto -\frac{1}{2} \mathbf{B}_k^T \mathbf{C}_{f_{\text{cl}}}^{-1} \mathbf{B}_k, \quad (34)$$

where  $\mathbf{B}_k = (B - B_{\text{model}})_k$  and  $\mathbf{C}_{f_{\text{cl}}}$  is the covariance matrix of the boost factor, also obtained from jackknife.

The weak-lensing and boost-factor profiles are fitted simultaneously with the total log-likelihood for a single cluster subset computed as

$$\begin{aligned} \ln L_k &= \ln L(\Delta\Sigma_k | M_k, p_{cc}, A_m, B_0, R_s) \\ &+ \ln L(f_{\text{cl},k} | B_0, R_s). \end{aligned} \quad (35)$$

Note that while the fit of  $\Delta\Sigma$  and boost factor is performed in conjunction, each cluster subset is fitted independently of the other subsets. Also, note that in our approach, the constraints on the boost-factor parameters are informed by both their dilution effect on the  $\Delta\Sigma$  profile (as shown in equation 32) and independent measurements of  $f_{\text{cl}}$  (see an example of such measurement in Fig. 5).

A list of the model parameters describing each cluster stack and their corresponding priors is summarized in Table 3. We use the Bayesian formalism and the Markov chain Monte Carlo (MCMC) method through the package EMCEE (Foreman-Mackey et al. 2013) to perform the likelihood sampling. We use 64 walkers with 10 000 steps each, discarding the first 2000 steps of each walker as burn-in. We also verify the autocorrelation time of the chains to check their convergence. To avoid confirmation bias, we blind the chains before applying the corrections of triaxiality and projections effects and model bias, which we will describe in the next section. Our blinding procedure relies on randomly shifting the peak of the posterior distribution of  $M_{200c}$  in the chains.

### 3.5 Modelling systematics

The analytical model for the centred term,  $\Delta\Sigma_{\text{NFW}}$  (Bartelmann 1996; Wright & Brainerd 2000), can present differences from the true  $\Delta\Sigma$  profiles of the cluster haloes of mean mass  $M$ . These deviations are due to the mismatch of density profiles in simulations (Melchior et al. 2017; Murata et al. 2018; McClintock et al. 2019), in particular, in the transition between the one- and two-halo regimes, which can bias the recovered weak-lensing masses. Therefore, we need to calibrate our model with simulations.

In order to achieve that, we measure the weak-lensing masses of dark matter haloes in  $N$ -body simulations using the same formalism we employ to the DES data. The haloes are drawn from a  $N$ -body simulation of a flat  $\Lambda$ CDM cosmology run with GADGET (Springel 2005). The simulation uses  $1400^3$  particles in a box with

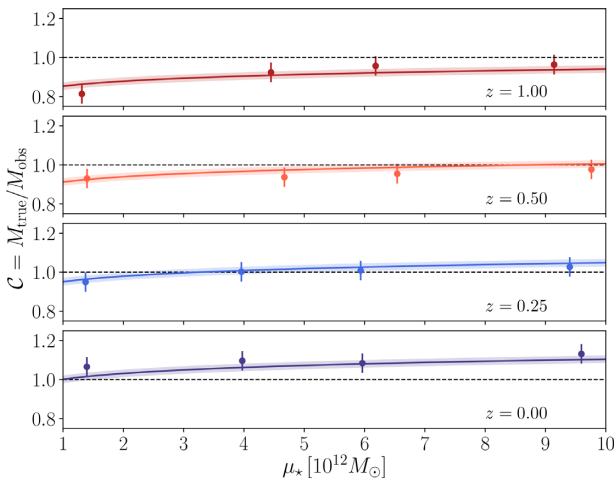


**Figure 7.** The mass bias calibration  $C = M_{\text{true}}/M_{\text{obs}}$ , caused by the adopted analytical form of the  $\Delta\Sigma$  profile, as a function of  $\mu_*$  for each simulated redshift bin. The solid line and shaded region are the best-fitting bias model from equation (36) and  $1\sigma$  uncertainty of the calibration, respectively. Error bars on the measured calibrations are the fitted intrinsic scatter  $\sigma_C$ . Here we multiply the error bars by a factor of 3 for a better visualization.

$1050 h^{-1}$  Mpc on a side with periodic boundary conditions. The force softening is  $20 h^{-1}$  kpc. The simulation was run with the cosmology  $\Omega_m = 0.318$ ,  $h = 0.6704$ ,  $\Omega_b = 0.049$ ,  $\tau = 0.08$ ,  $n_s = 0.962$ , and  $\sigma_8 = 0.835$ . Haloes of mass  $10^{13} h^{-1} M_\odot$  are resolved with 100 particles. Haloes are defined using a spherical overdensity mass definition of 200 times the background density and are identified with the ROCKSTAR halo finder (Behroozi, Wechsler & Wu 2013).

The simulation is used to construct the synthetic  $\Delta\Sigma$  profiles of haloes at four different snapshots:  $z \in [0, 0.25, 0.5, 1]$ . We assigned a  $\mu_*$  to each halo by inverting the mass– $\mu_*$  relation of Pereira et al. (2018) and adding 25 per cent scatter. Then, we grouped our haloes into  $(z, \mu_*)$  subsets identical to how we grouped our real clusters. For each of these halo subsets, we measured the halo–matter correlation function with the Landy & Szalay (1993) estimator implemented in the CORRFUNC  code (Sinha & Garrison 2017). We numerically integrate the halo–matter correlation function to obtain the  $\Delta\Sigma$  profile. The resulting simulated  $\Delta\Sigma$  profile is a combination of the  $\Delta\Sigma_{\text{NFW}}$  and a two-halo term.

Note that this  $\Delta\Sigma$  profile does not contain any of the systematics that exists in the real data. To incorporate the systematics, we modify the simulated  $\Delta\Sigma$  profiles by applying the corrections in equation (32). The miscentring profile  $\Delta\Sigma_{\text{misc}}$  is computed by providing as input the true mass from the simulation and the miscentring distribution discussed in Section 3.3.1. The values of  $p_{\text{cc}}$  and  $A_m$  are the central values described in Table 3. For the boost-factor correction  $B(R)$  described in Section 3.3.2, the values for  $B_0$  and  $R_s$  are obtained from modelling the boost-factors data independently. To apply the reduced shear correction  $G(R)$  described in Section 3.3.3 in the simulation we use the same  $\Sigma_{\text{crit}}^{-1}$  of the real data. Note that in the real data we just have three bins of redshifts; therefore, we repeat the values of the third  $z$ -bin for the snapshot with  $z = 1$  in the simulations.

We obtain the observed mass  $M_{\text{obs}}$  for this simulated profile by using the same pipeline we apply on the real data, restricting ourselves to the same radial scales employed in the weak-lensing analysis, and utilizing the covariance matrices recovered from the data to ensure that the simulated data are weighted in the same way as the observed data.

**Table 4.** Parameters in the model bias fit. Flat priors are specified with limits in square brackets.

Parameter	Description	Prior
$C_0$	Normalization	$[0, \infty]$
$\alpha$	Slope in $\mu_*$	$[-10, 10]$
$\beta$	Slope in $z$	$[-10, 10]$
$\ln(\sigma_C^2)$	Intrinsic scatter	$[-10, 10]$

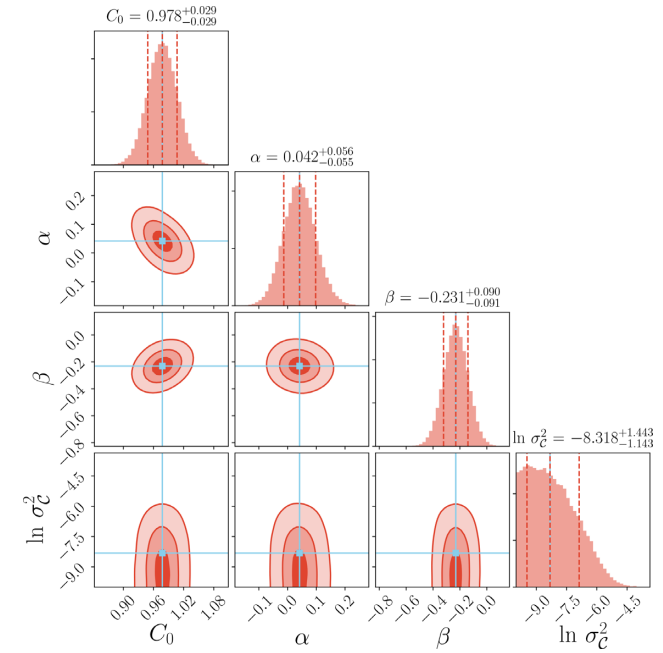


**Figure 8.** Parameters of the  $C(\bar{\mu}_*, z)$  relation in equation (36). Contours are the  $1\sigma$ ,  $2\sigma$ , and  $3\sigma$  confidence areas.

Defining  $M_{\text{true}}$  as the mean mass of the haloes in the simulated stack, the calibration for each simulated profile is shown in Fig. 7. The model bias calibration  $C = M_{\text{true}}/M_{\text{obs}}$  was modelled as a function of the mean  $\bar{\mu}_*$  and redshift snapshot  $z$  of the simulated stack as

$$C(\bar{\mu}_*, z) = C_0 \left( \frac{\bar{\mu}_*}{5.16 \times 10^{12} M_\odot} \right)^\alpha \left( \frac{1+z}{1+z_0} \right)^\beta, \quad (36)$$

with  $z_0 = 0.5$  as pivot redshift. The free parameters in the fit are  $C_0$ ,  $\alpha$ ,  $\beta$ , and the intrinsic scatter  $\sigma_C$  of the calibration, and they are determined via a Bayesian fit using flat priors for the parameters (see Table 4).

The mean model bias for our simulated stacks is  $\sim 5$  per cent with  $C_0 = 0.978 \pm 0.029$ ,  $\alpha = 0.042 \pm 0.055$ ,  $\beta = -0.231 \pm 0.090$ , and  $\text{intrinsic scatter } \sigma_C = 0.016$ . In Fig. 8 we show the contour plots for these parameters.

We repeated this analysis for profiles assuming different amounts of intrinsic scatter in the  $M-\mu_*$  relation from 10 up to 45 per cent. We found that the amount of model bias does not present a significant change with scatter in the  $M-\mu_*$  relation. We also have checked that the model bias has negligible changes when we consider the effect of selecting in  $\lambda$  but binning in  $\mu_*$ . To mimic this effect in the simulations, we populated the haloes with  $\lambda$  and  $\mu_*$ , by inverting the  $M-\lambda$  relation from Melchior et al. (2017) and the  $M-\mu_*$  relation from Pereira et al. (2018), with scatters  $\sigma_{M|\lambda}$  and  $\sigma_{M|\mu_*}$ . Then, we selected haloes with  $\lambda > 20$  and stacked them in bins of  $z$  and  $\mu_*$ , verifying the change in the model bias with the different scatters in the  $M-\mu_*$ .

**Table 5.** Best-fitting results for redMaPPer clusters in Fig. 3. In the fitting, we use a concentration–mass relation from Diemer & Joyce (2019) to fix  $c_{200c}$  and we also fix the width of miscentring distribution as  $\sigma_{\text{off}} = 0.133 h^{-1}$  Mpc. Our final model has five free parameters, namely the mass  $M_{200c}$ , the fraction of clusters that is correctly centred  $p_{\text{cc}}$ , the shear+photo- $z$  bias  $A_m$ , and the boost-factor parameters  $B_0$  and  $R_s$ . The weak-lensing and boost-factor profiles were fitted simultaneously, but each cluster subset is fitted independently of each other. We note that the posteriors of  $p_{\text{cc}}$  are dominated by the priors and one could say that the measurement is non-informative. However, since we are using the values determined by a previous measurement of the corrected centred redMaPPer cluster in comparison to an X-ray sample (Zhang et al. 2019a; von der Linden et al., in preparation), we believe that it is reasonable to assume that the used informative prior in  $p_{\text{cc}}$  will not bias the recovered masses. For convenience, we also present here the estimated masses converted to the definition  $M_{200m}$  by using the COLOSSUS code.

$\mu_*$ [ $10^{12} M_\odot$ ]	$z$	$M_{200c}$ [ $10^{14} h^{-1} M_\odot$ ]	$M_{200m}$ [ $10^{14} h^{-1} M_\odot$ ]	$p_{\text{cc}}$	$A_m$	$B_0$	$R_s$ [Mpc]
[0.0, 3.3)	[0.1, 0.33)	$0.70 \pm 0.06$	$0.90 \pm 0.08$	$0.73 \pm 0.08$	$1.019 \pm 0.024$	$0.59 \pm 0.21$	$0.20 \pm 0.06$
[3.3, 5.0)	–	$1.18 \pm 0.11$	$1.52 \pm 0.14$	$0.72 \pm 0.08$	$1.017 \pm 0.023$	$0.36 \pm 0.11$	$0.61 \pm 0.18$
[5.0, 7.5)	–	$1.38 \pm 0.12$	$1.77 \pm 0.15$	$0.69 \pm 0.08$	$1.016 \pm 0.024$	$0.40 \pm 0.08$	$0.63 \pm 0.13$
[7.5, 60.0)	–	$2.46 \pm 0.16$	$3.16 \pm 0.20$	$0.64 \pm 0.07$	$1.009 \pm 0.024$	$0.24 \pm 0.03$	$1.21 \pm 0.16$
[0.0, 4.04)	[0.33, 0.5)	$0.81 \pm 0.09$	$0.98 \pm 0.11$	$0.77 \pm 0.08$	$1.015 \pm 0.023$	$0.33 \pm 0.25$	$0.02 \pm 0.02$
[0.04, 5.65)	–	$0.89 \pm 0.10$	$1.07 \pm 0.12$	$0.76 \pm 0.08$	$1.015 \pm 0.023$	$0.26 \pm 0.20$	$0.14 \pm 0.09$
[5.65, 8.05)	–	$1.34 \pm 0.12$	$1.64 \pm 0.14$	$0.69 \pm 0.07$	$1.011 \pm 0.023$	$0.21 \pm 0.09$	$0.27 \pm 0.09$
[8.05, 60.0)	–	$2.24 \pm 0.14$	$2.73 \pm 0.17$	$0.74 \pm 0.07$	$1.012 \pm 0.023$	$0.07 \pm 0.02$	$0.86 \pm 0.23$
[0.0, 3.88)	[0.5, 0.65)	$0.66 \pm 0.12$	$0.77 \pm 0.14$	$0.75 \pm 0.08$	$1.015 \pm 0.025$	$0.33 \pm 0.25$	$0.03 \pm 0.02$
[3.88, 5.42)	–	$0.83 \pm 0.12$	$0.97 \pm 0.14$	$0.74 \pm 0.08$	$1.016 \pm 0.025$	$0.26 \pm 0.22$	$0.12 \pm 0.09$
[5.42, 7.68)	–	$1.09 \pm 0.14$	$1.28 \pm 0.16$	$0.74 \pm 0.08$	$1.016 \pm 0.025$	$0.09 \pm 0.10$	$0.33 \pm 0.25$
[7.68, 60.0)	–	$1.91 \pm 0.17$	$2.24 \pm 0.19$	$0.73 \pm 0.08$	$1.014 \pm 0.025$	$0.29 \pm 0.15$	$0.16 \pm 0.05$

relation. No relevant changes were found. So, we concluded that neither the selection effect of selecting in  $\lambda$  but ranking in  $\mu_*$  nor the different amount of scatters has significant impact in our model bias correction.

In our analysis, we focus on the modelling of the centred term by choosing a radial cut,  $R = (0.2\text{--}2.5)$  Mpc, to avoid the two-halo term and we use an analytical expression for the NFW profile. However, the simulated profiles were generated by an integration of the halo-matter correlation function that accounts both for the centred and two-halo contributions. This might be causing a significant model bias between our model and the simulated profiles, in particular, at the high redshifts snapshots  $z = 1$  as seen in Fig. 7. Besides that, we are not considering the effect of baryonic physics that might have some impact, especially in the central regions of the halo. Once we apply a radial cut in the inner profile before performing the fit, we expect to minimize the impact of baryonic effects as argued in McClintock et al. (2019). However, this will not be true for haloes that are miscentred by a large amount. The impact of baryonic effects could also be ‘absorbed’ by the concentration parameter  $c_{200}$ . However, in this work, we are fixing  $c_{200}$  by a Diemer & Joyce (2019) concentration. We have tested in some stacks this choice and found a change of  $\sim 7$  per cent of the recovered weak-lensing mass compared to varying  $c_{200}$ . Due to the computational time needed for the fitting code to converge, we then decided to keep our choice of a fixed  $c_{200}$  for this work. Thus, we note that our model calibration might be limited by this choice and further investigations are needed to properly account for the impact of baryonic physics, e.g. by using hydrodynamic simulations. We plan to investigate such effects in a forthcoming work, but for the current analysis we apply the model calibration as described in this section.

After this model calibration, the correction for the mean weak-lensing mass of a cluster stack in a given bin of  $\mu_*$  at redshift  $z$  should be

$$M' = C(\mu_*, z)M_{\text{WL}}, \quad (37)$$

where  $M_{\text{WL}}$  is the uncalibrated mass estimate and the calibration factor  $C(\mu_*, z)$  is determined by randomly picking one value from the simulation posteriors.

The final posteriors for our weak-lensing masses are properly marginalized over the uncertainty in the calibration factor  $C$  as well as triaxiality and projection effects such that

$$M = G(0.96, 0.02) \times G(1.02, 0.02) \times M' \quad (38)$$

after fitting the lensing and boost-factor data but before modelling the mass– $\mu_*$ – $z$  relation. The final unblinded and corrected masses are shown in Table 5.

#### 4 THE MASS– $\mu_*$ –REDSHIFT RELATION

We obtain a mass calibration for the galaxy cluster stacks using their weak-lensing masses shown in Table 5. We characterize the mass– $\mu_*$ –redshift relation of these clusters as

$$\langle M | \mu_*, z \rangle = M_0 \left( \frac{\mu_*}{\mu_*^0} \right)^{F_{\mu_*}} \left( \frac{1+z}{1+z_0} \right)^{G_z}, \quad (39)$$

where  $M_0$ ,  $F_{\mu_*}$ , and  $G_z$  are the free parameters of our model with pivot values  $\mu_*^0 = 5.16 \times 10^{12} M_\odot$  and  $z_0 = 0.35$ . We model the likelihood for our model as

$$\ln L(M_{\text{obs}} | M_0, F_{\mu_*}, G_z) \propto -\frac{1}{2} (\Delta M)^T \mathbf{C}_M^{-1} (\Delta M), \quad (40)$$

where  $\Delta M = M - \langle M | \mu_*, z \rangle$ . Here, the mass  $M$  is the value after unblinding and applying the correction in equation (38).  $\mathbf{C}_M$  is the covariance matrix between the mass bins obtained following section 6.2 of McClintock et al. (2019).

Briefly, to construct the mass covariance, we combine the errors in the mass obtained by performing the profile fitting in three configurations: (i) our fiducial run called `Full`, where we vary all the five parameters of our lensing likelihood using the priors in Table 3, and for which the posteriors are reported in Table 5; (ii) `FixAm`, where the shear+photo- $z$  parameter  $A_m$  is fixed to 1 and the other four parameters are free; (iii) `OnlyM`, where the only free parameter is the mass. We do not report the posteriors for `FixAm` or `OnlyM` configurations.

Besides being used for constructing the full mass covariance, we can perform the mass calibration for each of these configurations and use the estimated uncertainties in each parameter to determine the

**Table 6.** Parameters of the  $M-\mu_{\star}-z$  relation from equation (40) with their posteriors. The mass is defined as  $M_{200c}$  in units of  $h^{-1} M_{\odot}$ . The pivot  $\mu_{\star}$  and pivot redshift correspond to the median values of the cluster sample. Flat priors are specified with limits in square brackets. Uncertainties are the  $1\sigma$  confidence intervals and are split into statistical (first) and systematic (second). The posterior of  $M_0$  is in units of  $h^{-1} M_{\odot}$ .

Parameter	Description	Prior	Posterior
$M_0$	Mass pivot	$[10^{11}, 10^{18}]$	$1.14 \pm 0.05 \pm 0.05$
$F_{\mu_{\star}}$	Mass proxy scaling	$[-10, 10]$	$0.76 \pm 0.01 \pm 0.06$
$G_z$	Redshift scaling	$[-10, 10]$	$-1.14 \pm 0.04 \pm 0.38$

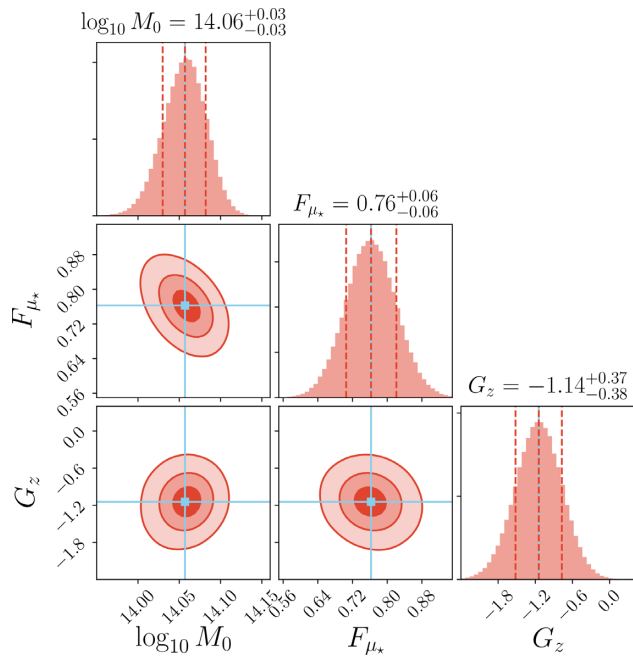


**Figure 9.** Parameters of the  $M_{200c}-\mu_{\star}-z$  relation. Contours show the  $1\sigma$ ,  $2\sigma$ , and  $3\sigma$  confidence areas from the fiducial FULL run. At the top label, we show the  $1\sigma$  total uncertainties. For easy comparison with other results in the literature, we are plotting  $\log_{10}M_0$  converted from  $M_0$ , in which we performed the fit.

statistical and systematic uncertainties in our final mass calibration. The statistical error is computed by the difference in the variance of the parameters obtained with the masses from Full and FixAm configurations. The systematic uncertainties are obtained by the difference in the parameter's variance between the Full and OnlyM.

Our final mass calibration is performed using the masses from our fiducial Full configuration together with the mass covariance described in this section. The posteriors of the fitted parameters are summarized in Table 6. The corresponding confidence contours are shown in Fig. 9. This result shows that a galaxy cluster with  $\mu_{\star} = 5.16 \times 10^{12} M_{\odot}$  at  $z = 0.35$  has a mean mass of  $\log_{10}M_{200c} = 14.06 \pm 0.03$ .

For a direct comparison with our previous work (Pereira et al. 2018), we show in Fig. 10 our estimated  $M_{200m}-\mu_{\star}-z$  relation (blue, grey, and red solid lines) and the corresponding  $1\sigma$  confidence intervals (blue, grey, and red shaded regions) for redMaPPer clusters in DES Y1 overlapped with the  $2\sigma$  confidence intervals (orange shaded regions) for the mass calibration of CS82's redMaPPer clusters.

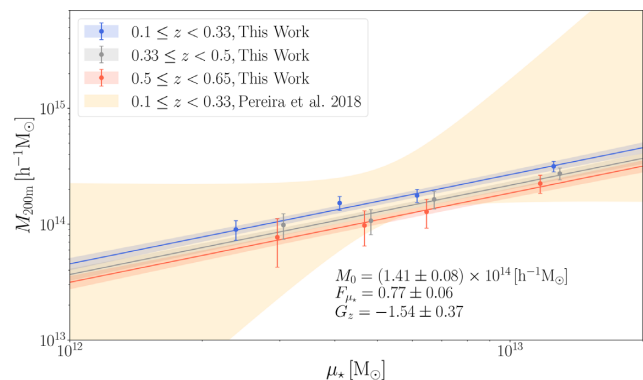


**Figure 10.** The mass calibration in three redshift bins for the mass definition  $M_{200m}$  in units of  $h^{-1} M_{\odot}$ . The solid lines are the result of our best fit with the corresponding  $1\sigma$  confidence intervals as shaded regions. For comparison, we also present the  $2\sigma$  confidence intervals of the previous mass calibration of Pereira et al. (2018) as the orange shaded region.

## 5 RESULTS

We perform a weak-lensing mass calibration of the total stellar-mass-based mass proxy  $\mu_{\star}$  using DES Y1 redMaPPer clusters. We divide our sample into 12 stacks binned by redshift and  $\mu_{\star}$  in the range  $0.1 \leq z < 0.65$ ,  $\mu_{\star} < 5.5 \times 10^{13} M_{\odot}$ , using the sample with  $\lambda > 20$ . Therefore, we use the same redMaPPer-selected cluster sample as in McClintock et al. (2019), but compute  $\mu_{\star}$  for each of the identified clusters and perform the weak-lensing analysis binning in this new proxy.

We model the weak-lensing signal by taking into account: cluster miscentring (Section 3.3.1); model calibration systematics (Section 3.5); source sample dilution by cluster members (Section 3.3.2); shear measurement systematics and source photometric redshift uncertainties (Section 3.3.3, Section 3.3.4); and triaxiality and projection effects (Section 3.3.5). We perform the modelling of the weak-lensing signal and apply a blinding factor in the derived posterior of the masses to avoid confirmation bias in our estimates.

We performed the unblinding after reaching the final version of our modelling pipeline [b3](#), which was validated by an internal review from members of the DES collaboration prior to unblinding. No changes to the analysis and modelling pipeline were made post-unblinding.

We use the derived average masses to determine the cluster mass calibration of  $M_{200c}$  as a function of  $\mu_{\star}$  and redshift according to equation (39). The summary of our constraints on the scaling relation for clusters at pivots  $\mu_{\star}^0 = 5.16 \times 10^{12} M_{\odot}$  and  $z_0 = 0.35$  is a mean cluster mass of

$$M_0 = [1.14 \pm 0.05 \pm 0.05] \cdot 10^{14} h^{-1} M_{\odot}, \quad (41)$$

with the slope  $F_{\mu_{\star}}$  for the mass proxy's term of

$$F_{\mu_{\star}} = 0.76 \pm 0.01 \pm 0.06, \quad (42)$$

and the slope  $G_z$  for the redshift's term of

$$G_z = -1.14 \pm 0.04 \pm 0.38, \quad (43)$$

where the first and second terms in the errors correspond to statistical and systematic, respectively.

## 6 DISCUSSION

Here we present a detailed discussion of the relationship between  $\mu_{\star}$  and  $\lambda$  to check the impact on the MOR of our  $\lambda$ -selected sample binned in  $\mu_{\star}$ . We also discuss our findings in the context

of our previous work and present some possible ways to use  $\mu_*$  for applications in cluster cosmology.

### 6.1 The relationship between $\lambda$ and $\mu_*$ and implications for the slope $F_{\mu_*}$

In this section, we describe how to build a model for the relationship between  $\lambda$  and  $\mu_*$  from simulations to check for potential selection effects. We start with a dark matter halo catalogue from a simulation of sufficient scale to contain rare massive haloes. As our work uses a  $\lambda \geq 20$  catalogue to bin in  $\mu_*$ , we will need to assign each halo  $\mu_*$  and  $\lambda$ .

Following Rozo et al. (2014), Evrard et al. (2014), Simet et al. (2017), and Oguri et al. (2018), we assume that the relationship of mass and an observable  $s$  follows a power-law form. For  $\lambda$ , this  $\langle \log M | s \rangle$  is

$$\langle \log M | \lambda \rangle = a \log \left( \frac{\lambda}{40} \right) + b, \quad (44)$$

where from McClintock et al. (2019) we have  $a = 1.36 \pm 0.05$ ,  $b = 14.49 \pm 0.02$  (we will assume that redshift evolution is zero), and from Farahi et al. (2019) we have  $\sigma_{\log M | \lambda} = 0.13$ . For  $\mu_*$ , the relation is

$$\langle \log M | \mu_* \rangle = a \log \left( \frac{\mu_*}{5.2 \times 10^{12}} \right) + b, \quad (45)$$

where from this paper we have  $a = 0.77 \pm 0.06$ ,  $b = 14.30 \pm 0.02$ , and by converting the scatter from Palmese et al. (2020) to logarithmic base 10, we have  $\sigma_{\log M | \mu_*} = 0.11$ . Note that we have made the proper conversions of these results to work with masses from simulations that are in units of  $M_{200m} [\text{M}_\odot]$ .

To assign properties to our dark matter haloes, we will need  $p(\log \mathbf{s} | M)$ , where  $\mathbf{s}$  is our vector of observables, i.e.  $\mathbf{s} = \{\lambda, \mu_*\}$ . Following Evrard et al. (2014) and Oguri et al. (2018), through the Bayes theorem  $p(\log M | \mathbf{s})$  can be converted to  $p(\log \mathbf{s} | M)$  by

$$p(\log \mathbf{s} | M) = \frac{p(\log M | \mathbf{s}) p(\log \mathbf{s})}{\int d(\log \mathbf{s}) p(\log M | \mathbf{s}) p(\log \mathbf{s})}. \quad (46)$$

Using the locally power-law model of Rozo et al. (2014) and Evrard et al. (2014), we find that this has a lognormal distribution with mean

$$\langle \log \mathbf{s} | M \rangle = [\boldsymbol{\alpha}^T \mathbf{C}^{-1} (\mu - \boldsymbol{\pi}) - \boldsymbol{\beta} \ln(10)] \sigma_{\log \mathbf{s} | M}^2, \quad (47)$$

and variance

$$\sigma_{\log \mathbf{s} | M}^2 = (\boldsymbol{\alpha}^T \mathbf{C}^{-1} \boldsymbol{\alpha})^{-1}, \quad (48)$$

where  $\boldsymbol{\alpha} = \{a_\lambda, a_{\mu_*}\}$ ,  $\mu = \log M$ ,  $\boldsymbol{\pi} = \{b_\lambda, b_{\mu_*}\}$ , and  $\boldsymbol{\beta}$  is the slope of the observable's function. For  $\lambda$ , this is  $p(\log \lambda) \propto \lambda^{-\beta}$ . Working iteratively, we find that  $\beta_\lambda = 3.5$  and  $\beta_{\mu_*} = 1.67$  for mocks near thresholds of interest. The elements of the covariance matrix  $\mathbf{C}$  are computed by  $C_{ij} = r_{ij} \sigma_i \sigma_j$ , where  $r$  is the correlation coefficient between  $\lambda$  and  $\mu_*$ . The scatters  $\sigma$  are given by the components  $\{\sigma_{\log \lambda | M}, \sigma_{\log \mu_* | M}\}$ .

We took the halo catalogue from the DES Buzzard simulation v1.9.2 (DeRose et al. 2019), selecting a total of 16 000 square deg. We paint on the observables accounting for the correlation between them: To a given halo, each observable  $\mathbf{s}$  has a property computed via equation (47) with a random normal deviation given by equation (48).

The mock catalogue is used to construct observable vectors that may be compared against data or simulations. To verify whether our observable vectors are reliable, we can check: (i) the observed  $p(\lambda | \mu_*)$  and (ii) the fraction  $p(\log \mu_* - M | \log M)$ . We will start with

the latter. The stellar mass in clusters is known to be a few per cent of the halo dark matter mass. In the simulations studied by Farahi et al. (2018), fig. 3 shows a  $p(\log M_* - M | \log M)$  that goes from 2 to 1 per cent over the mass range of interest. We note here that in their work they use the stellar mass  $M_*$  and not  $\mu_*$ , but since we derived  $\mu_*$  from stellar mass, we expect to recover similar values for the stellar fraction computed with  $\mu_*$ , i.e.  $p(\log \mu_* - M | \log M)$ . Using equation (47), we can paint stellar masses on top of dark matter haloes. In order to recreate a physical behaviour for the  $p(\log \mu_* - M | \log M)$  relation of haloes with  $\log M / M_\odot \approx 14.30$ , the value for the slope needs to be between  $F_{\mu_*} \approx 0.75$  and 1. We checked that values of  $F_{\mu_*}$  lower than this (e.g.  $\sim 0.5$ ) start to deviate from what is known about the cluster stellar fractions.

A mock catalogue generated using values for the pivot mass and the mass proxy scaling for  $\mu_*$  that recreates the cluster stellar fractions in the simulations of Farahi et al. (2018) and the scaling relation of McClintock et al. (2019) for  $\lambda$ , then reproduces the observed  $p(\lambda | \mu_*)$  relation in the log-space, that is

$$\log \lambda = (-5.06 \pm 0.17) + (0.52 \pm 0.01) \log \mu_*, \quad (49)$$

with an intrinsic scatter of  $\sigma_{\lambda | \mu_*} = 0.16$ . For the mocks, performing a simple linear fit with PYTHON POLYFIT, we obtained a relation that is  $\log \lambda = (-6.42 \pm 0.02) + (0.626 \pm 0.002) \log \mu_*$ , with a scatter of  $\sigma_{\lambda | \mu_*} = 0.08$ . Therefore, when using the fitted intrinsic scatter  $\sigma_{\lambda | \mu_*}$  as the  $1\sigma$  uncertainty of the mean relation, the derived observed and simulated relations are in good agreement.

Having produced acceptable mocks, we can explore the question of the effect of selecting on  $\lambda > 20$  on the slope of the  $\langle \log M | \mu_*, z \rangle$  relation measured by weak lensing having stacked in  $\mu_*$ .

In order to do this, we divided the haloes into three bins of  $z$  [0.1–0.33, 0.33–0.5, 0.5–0.65] and four of  $\mu_*$  [0.5–3, 3–5, 5–10, 10–100]  $\times 10^{12} \text{ M}_\odot$  for samples that have cuts of  $\lambda \geq [0, 10, 20]$ . We took the average values of  $M$ ,  $\mu_*$ , and  $z$  in these bins and then performed an MCMC fit in the same form we did in real data. We found that the slope between the lowest and second  $\lambda$ -cut is basically unaffected, changing by  $\sim 2$  per cent. The slope between the second and third  $\lambda$ -cut changed by  $\sim 7$  per cent. Considering the error bars from the MCMC, we can see that this change in the slope is not too significant. In summary, we believe that selecting on one observable and binning on another should have an effect (e.g. changes in the slope), but looking into simulations that reliably reproduce our observables, we find that there was no significant change in the slope when we mimic this selection. Therefore, we do not believe that there is a significant signal of this selection effect in our results. Secondly, for plausible stellar mass fractions, i.e.  $p(\log \mu_* - M | \log M)$  relations, one expects power-law relations for  $\langle \log M | \mu_* \rangle$  to have exponents between 0.75 and 1, which is consistent with the slope of 0.77 that we found in our data.

### 6.2 The redshift evolution of the $M - \mu_* - z$ relation

The  $M - \mu_* - z$  relation presented in the Section 5 shows a marginal dependence on redshift.  $G_z$  is in fact  $3\sigma$  away from the  $G_z = 0$  case. However, as can be noted from Fig. 10, there is a 0.1–0.2 dex difference in  $\mu_*$  at fixed  $M_{200m}$  between the lowest and highest redshift bins. This number is consistent with the typical intrinsic scatter in stellar mass at fixed halo mass (e.g. Pillepich et al. 2018), implying that the found redshift evolution is not significant. The stellar mass functions in DES galaxy clusters studied in Palmese et al. (in preparation) also find no significant redshift evolution, using the same stellar masses.

Given the current uncertainties, the simple redshift evolution model used in this work is appropriate, but for future analyses with DES clusters including larger statistics, a more sophisticated model shall be tested. In fact, Farahi et al. (2018) showed that the slope and scatter in the stellar mass–halo mass relation show some evidence for running with  $z$ , although this is not as strong of an effect as the one found for the gas fraction.

When comparing our result to the literature, one should also note that intra-cluster light (ICL) is not taken into account in this work, since simulation studies will often include the diffuse component when quoting the total stellar mass. The ICL can constitute a significant fraction of the total stellar mass (up to 40 per cent, e.g. Pillepich et al. 2018 and Zhang et al. 2019b), and it has been shown to build up since  $z \sim 1$  (e.g. Burke, Hilton & Collins 2015).

### 6.3 Comparison with previous work and considerations about selection effects

The comparison of the result obtained in this work with a previous calibration of  $\mu_*$  at low redshifts is tricky, because there we used a different cluster sample identified by redMaPPer and Voronoi-Tessellation cluster finders in the SDSS Stripe 82 region, and we assumed an MOR without redshift evolution. For SDSS redMaPPer clusters, we found a slope for the mass proxy of  $1.74 \pm 0.62$ , which is compatible at  $\sim 2\sigma$  with our present result.

It is known that at  $z < 0.1$ , nearly all cluster members are red (e.g. Aguerri, Sánchez-Janssen & Muñoz-Tuñón 2007). However, at higher redshifts ( $z > 0.1$ ), the number of blue galaxies is observed to increase and the number of red members is observed to decrease (e.g. Butcher & Oemler 1984; Rakos & Schombert 1995; Gerke et al. 2007; Nishizawa et al. 2018). Furthermore, at low  $z$  almost all galaxies more massive than  $10^{10.3} M_\odot$  are red, and this corresponds roughly to the  $0.4 L_*$  luminosity threshold of redMaPPer. Thus, at low  $z$ ,  $\lambda$ , and  $\mu_*$  red-sequence-selected samples should have, approximately, the same number of total members and the same stellar mass. At higher  $z$ , richness and stellar mass are expected to evolve differently. We believe that this effect is related to the evidence for redshift evolution in our MOR results (as the redshift slope  $G_z$  is not consistent with zero; see Section 6.2) that is not observed in McClintock et al. (2019). In fact, previous works (e.g. Farahi et al. 2018) have found evidence that the stellar mass content of clusters may evolve with redshift.

We have checked that the potential selection effect on  $\langle M | \mu_*, z \rangle$  introduced by the fact that the cluster sample has been selected with a cut in richness at  $\lambda > 20$  is subdominant for our results (see Section 6.1). In fact, in the absence of scatter between  $\lambda$  and  $\mu_*$ , selecting in  $\lambda$  or in  $\mu_*$  would have the same meaning. However, Palmese et al. (in preparation) find that the scatter in  $\mu_*$  at fixed richness is  $\sigma_{\mu_*|\lambda} \sim 0.25$  dex for the  $\lambda > 5$  sample, result that is largely dominated by the scatter at the low-richness end ( $\lambda < 20$ ). The largest impact of this scatter on our result is expected to be at the lowest  $\mu_*$  binning, where some clusters may have scattered to  $\lambda < 20$ . We tested the impact of this effect by removing from our fit the lowest  $\mu_*$  binning, and found no significant change in our parameter estimates of the MOR.

With this work, we complete the programme of establishing  $\mu_*$  as a reliable mass proxy in the same regime as the  $\lambda$ -based mass calibration work by the DES collaboration, opening the possibility of exploring the novel regimes of low mass–low  $z$  and high mass–high  $z$  in a forthcoming paper.

### 6.4 Possible implications for cluster cosmology

Since there is a tight connection between galaxy masses and halo masses (e.g. Conroy & Wechsler 2009; Behroozi, Conroy & Wechsler 2010; Coupon et al. 2015; Niemiec et al. 2017; Shan et al. 2017; Wechsler & Tinker 2018; Huang et al. 2020; Palmese et al. in preparation), stellar-mass-based mass proxies such as  $\mu_*$  show great potential to be accurate halo mass estimators in photometric galaxy surveys. They can be used to probe galaxy evolution and can also help to improve the constraints on cosmological parameters.

In the review by Wechsler & Tinker (2018), they present a series of application for the galaxy–halo connection in cosmology, e.g. systematics in cluster cosmology, the impact of baryons, and galaxy clustering at small scales. For cluster cosmology, in particular, several studies have shown that projection effects have a non-negligible impact on the mass–richness relationship (Wojtak et al. 2018; Costanzi, M. and Rozo, E. et al. 2019b; Murata et al. 2019; Sunayama et al. 2020), most likely due to a dependence on the details of the galaxy–halo connection, such as the colour dependence of the cluster members. Since  $\mu_*$  is a colour-independent proxy and has a well-defined physical interpretation, we believe it has the potential to contribute in the understanding of the projection effects in the cluster cosmology context. In a future work, we plan to perform a comparison of projection effects between  $\mu_*$  and  $\lambda$ , using the new version of the DES Buzzard simulation (DeRose et al. 2019) that has stellar-mass information.

## 7 SUMMARY

We have measured the stacked weak-lensing signal around 6124 clusters in the DES Y1 redMaPPer catalogue with  $\lambda > 20$  and  $0.1 \leq z < 0.65$ . We have computed the stellar-mass-based proxy  $\mu_*$  for these clusters and performed the lensing measurements in bins of  $\mu_*$  and  $z$ . In the mass modelling, we have accounted for several systematics including cluster miscentring, model calibration, boost factors, shear and photo- $z$  bias, triaxiality, and projection effects.

Then, we use the fitted weak-lensing mass to perform the mass calibration of this sample. We find a mass– $\mu_*$ – $z$  relation of

$$\langle M_{200c} | \mu_*, z \rangle = 1.14 \pm 0.05 \text{ stat.} \pm 0.05 \text{ sys.} \cdot 10^{14} \times \left( \frac{\mu_*}{5.16 \times 10^{12} M_\odot} \right)^{0.76 \pm 0.01 \text{ stat.} \pm 0.06 \text{ sys.}} \times \left( \frac{1+z}{1.35} \right)^{-1.14 \pm 0.04 \text{ stat.} \pm 0.38 \text{ sys.}}, \quad (50)$$

in units of  $h^{-1} M_\odot$ . This scaling relation is consistent within  $2\sigma$  with previous  $\mu_*$  measurements using the SDSS redMaPPer clusters and lensing data from the CS82 survey (Pereira et al. 2018).

We have used mock catalogues from DES Buzzard simulations to check for a signal of selection effects since we have a  $\lambda$ -selected sample binned in  $\mu_*$ , but we found that such signal is negligible. We also concluded that if such an effect is present, we should have seen a considerable change in the slope due to the lowest  $\mu_*$  bin in comparison to the other bins. We test this hypothesis in the data by removing the lowest bin of  $\mu_*$  and performing the mass calibration again. We found no significant change in the slope of our relation. Therefore, we conclude that our analysis is not significantly affected by this selection effect. However, we understand that further work to properly quantify this selection effect is necessary. We also show from these mocks that shallower slopes in the mass proxy term are possible for stellar-mass-based proxies.

We found evidence for redshift evolution in our scaling relation. However, the difference in  $\mu_*$  at fixed halo mass between the lowest and highest redshift bins is  $\sim 0.1\text{--}0.2$  dex, which is consistent with intrinsic scatter in stellar mass at fixed halo mass, and this implies that the redshift evolution we found might not be significant.

This work provides the most careful weak-lensing mass calibration of  $\mu_*$  to date. It is an important step towards establishing  $\mu_*$  as a reliable mass proxy not only for studying systematics such as projection effects and low-richness clusters but also for future applications in cluster cosmology.

## ACKNOWLEDGEMENTS

This paper has been internally evaluated against a set of pass/fail criteria to give us confidence in its correctness prior to unblinding. MESP thanks Ben Lillard and Felix Kling for comments on the manuscript.

Funding for the DES Projects has been provided by the U.S. Department of Energy, the U.S. National Science Foundation, the Ministry of Science and Education of Spain, the Science and Technology Facilities Council of the United Kingdom, the Higher Education Funding Council for England, the National Center for Supercomputing Applications at the University of Illinois at Urbana-Champaign, the Kavli Institute of Cosmological Physics at the University of Chicago, the Center for Cosmology and Astro-Particle Physics at the Ohio State University, the Mitchell Institute for Fundamental Physics and Astronomy at Texas A&M University, Financiadora de Estudos e Projetos, Fundação Carlos Chagas Filho de Amparo à Pesquisa do Estado do Rio de Janeiro, Conselho Nacional de Desenvolvimento Científico e Tecnológico and the Ministério da Ciência, Tecnologia e Inovação, the Deutsche Forschungsgemeinschaft, and the Collaborating Institutions in the DES. The Collaborating Institutions are Argonne National Laboratory, the University of California at Santa Cruz, the University of Cambridge, Centro de Investigaciones Energéticas, Medioambientales y Tecnológicas-Madrid, the University of Chicago, University College London, the DES-Brazil Consortium, the University of Edinburgh, the Eidgenössische Technische Hochschule (ETH) Zürich, Fermi National Accelerator Laboratory, the University of Illinois at Urbana-Champaign, the Institut de Ciències de l'Espai (IEEC/CSIC), the Institut de Física d'Altes Energies, Lawrence Berkeley National Laboratory, the Ludwig-Maximilians-Universität München and the associated Excellence Cluster Universe, the University of Michigan, the National Optical Astronomy Observatory, the University of Nottingham, The Ohio State University, the University of Pennsylvania, the University of Portsmouth, SLAC National Accelerator Laboratory, Stanford University, the University of Sussex, Texas A&M University, and the OzDES Membership Consortium. Based in part on observations at CTIO, National Optical Astronomy Observatory, which is operated by the Association of Universities for Research in Astronomy (AURA) under a cooperative agreement with the National Science Foundation.

The DES data management system is supported by the National Science Foundation under Grant Numbers AST-1138766 and AST-1536171. The DES participants from Spanish institutions are partially supported by MINECO under grants AYA2015-71825, ESP2015-66861, FPA2015-68048, SEV-2016-0588, SEV-2016-0597, and MDM-2015-0509, some of which include ERDF funds from the European Union. IFAE is partially funded by the CERCA programme of the Generalitat de Catalunya. Research leading to these results has received funding from the European Research Council under the European Union's Seventh Frame-

work Programme (FP7/2007-2013) including ERC grant agreements 240672, 291329, and 306478. We acknowledge support from the Brazilian Instituto Nacional de Ciência e Tecnologia (INCT) e- Universe (CNPq grant 465376/2014-2).

This manuscript has been authored by Fermi Research Alliance, LLC under Contract No. DE-AC02-07CH11359 with the U.S. Department of Energy, Office of Science, Office of High Energy Physics.

## DATA AVAILABILITY

The data underlying this article are available in the DES Y1 data release page at <https://des.ncsa.illinois.edu/releases/y1a1/key-catalogs>.

## REFERENCES

Abbott T. M. C. et al., 2018a, *Phys. Rev. D*, 98, 043526  
 Abbott T. M. C. et al., 2018b, *ApJS*, 239, 18  
 Abbott T. M. C. et al., 2020, *Phys. Rev. D*, 102, 023509  
 Aguerri J. A. L., Sánchez-Janssen R., Muñoz-Tuñón C., 2007, *A&A*, 471, 17  
 Allen S. W., Evrard A. E., Mantz A. B., 2011, *ARA&A*, 49, 409  
 Andreon S., 2012, *A&A*, 548, A83  
 Angulo R. E., Springel V., White S. D. M., Jenkins A., Baugh C. M., Frenk C. S., 2012, *MNRAS*, 426, 2046  
 Annis J. et al., 2014, *ApJ*, 794, 120  
 Applegate D. E. et al., 2014, *MNRAS*, 439, 48  
 Ascaso B. et al., 2016, *MNRAS*, 456, 4291  
 Ascaso B., Mei S., Bartlett J. G., Benítez N., 2017, *MNRAS*, 464, 2270  
 Bartelmann M., 1996, *A&A*, 313, 697  
 Bartelmann M., Schneider P., 2001, *Phys. Rep.*, 340, 291  
 Behroozi P. S., Conroy C., Wechsler R. H., 2010, *ApJ*, 717, 379  
 Behroozi P. S., Wechsler R. H., Wu H.-Y., 2013, *ApJ*, 762, 109  
 Bellagamba F. et al., 2019, *MNRAS*, 484, 1598  
 Benítez N., 2000, *ApJ*, 536, 571  
 Bradshaw C., Leauthaud A., Hearin A., Huang S., Behroozi P., 2020, *MNRAS*, 493, 337  
 Brammer G. B. et al., 2009, *ApJ*, 706, L173  
 Burke C., Hilton M., Collins C., 2015, *MNRAS*, 449, 2353  
 Butcher H., Oemler A., Jr, 1984, *ApJ*, 285, 426  
 Carlstrom J. E. et al., 2011, *PASP*, 123, 568  
 Cecchi R., Bolzonella M., Cimatti A., Girelli G., 2019, *ApJ*, 880, L14  
 Chauke P. et al., 2019, *ApJ*, 877, 48  
 Coe D., Benítez N., Sánchez S. F., Jee M., Bouwens R., Ford H., 2006, *AJ*, 132, 926  
 Conroy C., Gunn J. E., 2010, *ApJ*, 712, 833  
 Conroy C., Wechsler R. H., 2009, *ApJ*, 696, 620  
 Costanzi M. et al., 2019a, *MNRAS*, 482, 490  
 Costanzi M. et al., 2019b, *MNRAS*, 488, 4779  
 Coupon J. et al., 2015, *MNRAS*, 449, 1352  
 Darvish B., Mobasher B., Sobral D., Rettura A., Scoville N., Faisst A., Capak P., 2016, *ApJ*, 825, 113  
 Davé R., Rafieferantsoa M. H., Thompson R. J., 2017, *MNRAS*, 471, 1671  
 DeRose J. et al., 2019, preprint ([arXiv:1901.02401](https://arxiv.org/abs/1901.02401))  
 Diehl H. T. et al., 2014, in Alison B. P., Chris R. B., Robert L. S., eds, *Proc. SPIE Conf. Ser. Vol. 9149, Observatory Operations: Strategies, Processes, and Systems V*. SPIE, Bellingham, p. 91490V  
 Diemer B., 2015, Colossus: COsmology, haLO, and large-Scale StrUcture tools, Astrophysics Source Code Library, record ascl:1501.016  
 Diemer B., Joyce M., 2019, *ApJ*, 871, 168  
 Dietrich J., 2016, NFW: NFW v0.1. available at: <https://doi.org/10.5281/zenodo.50664>  
 Dietrich J. P. et al., 2014, *MNRAS*, 443, 1713  
 Dietrich J. P. et al., 2019, *MNRAS*, 483, 2871  
 Dodelson S., Heitmann K., Hirata C., Honscheid K., Roodman A., Seljak U., Slosar A., Trodden M., 2016, preprint ([arXiv:1604.07626](https://arxiv.org/abs/1604.07626))

Drlica-Wagner A. et al., 2018, *ApJS*, 235, 33

Efron B., 1982, The Jackknife, the Bootstrap and Other Resampling Plans, CBMS-NSF Regional Conference Series in Applied Mathematics. Society for Industrial and Applied Mathematics, Philadelphia

Ettori S., Meneghetti M., 2013, *Space Sci. Rev.*, 177, 1

Evrard A. E., Arnault P., Huterer D., Farahi A., 2014, *MNRAS*, 441, 3562

Farahi A., Evrard A. E., McCarthy I., Barnes D. J., Kay S. T., 2018, *MNRAS*, 478, 2618

Farahi A. et al., 2019, *MNRAS*, 490, 3341

Feldmann R., Hopkins P. F., Quataert E., Faucher-Giguère C.-A., Kereš D., 2016, *MNRAS*, 458, L14

Flaugher B. et al., 2015, *AJ*, 150, 150

Ford J., 2016, Cluster-Lensing: v0.1.2. available at: <http://dx.doi.org/10.5281/zenodo.51370>

Ford J., VanderPlas J., 2016, *AJ*, 152, 228

Ford J., Hildebrandt H., Van Waerbeke L., Erben T., Laigle C., Milkeraitis M., Morrison C. B., 2014, *MNRAS*, 439, 3755

Ford J. et al., 2015, *MNRAS*, 447, 1304

Foreman-Mackey D., Hogg D. W., Lang D., Goodman J., 2013, *PASP*, 125, 306

George M. R. et al., 2012, *ApJ*, 757, 2

Gerke B. F. et al., 2007, *MNRAS*, 376, 1425

Girardi L., Bressan A., Bertelli G., Chiosi C., 2000, *A&AS*, 141, 371

Girelli G., Bolzonella M., Cimatti A., 2019, *A&A*, 632, A80

Gruen D., Brimioule F., 2017, *MNRAS*, 468, 769

Haiman Z., Mohr J. J., Holder G. P., 2001, *ApJ*, 553, 545

Harvey D., Massey R., Kitching T., Taylor A., Tittley E., 2015, *Science*, 347, 1462

Harvey D., Robertson A., Massey R., McCarthy I. G., 2019, *MNRAS*, 488, 1572

Hoekstra H., Herbonnet R., Muzzin A., Babul A., Mahdavi A., Viola M., Cacciato M., 2015, *MNRAS*, 449, 685

Hoeting J. A., Madigan D., Raftery A. E., Volinsky C. T., 1999, *Stat. Sci.*, 14, 382

Hoyle B. et al., 2018, *MNRAS*, 478, 592

Huang S. et al., 2020, *MNRAS*, 492, 3685

Huff E., Mandelbaum R., 2017, preprint ([arXiv:1702.02600](https://arxiv.org/abs/1702.02600))

Johnston D. E. et al., 2007, preprint ([arXiv:0709.1159](https://arxiv.org/abs/0709.1159))

Kim S. Y., Peter A. H. G., Wittman D., 2017, *MNRAS*, 469, 1414

Kneib J.-P. et al., 2003, *ApJ*, 598, 804

Kravtsov A. V., Borgani S., 2012, *ARA&A*, 50, 353

Kravtsov A. V., Vikhlinin A. A., Meshcheryakov A. V., 2018, *Astron. Lett.*, 44, 8

Landy S. D., Szalay A. S., 1993, *ApJ*, 412, 64

Leauthaud A. et al., 2017, *MNRAS*, 467, 3024

Mantz A. B. et al., 2015, *MNRAS*, 446, 2205

Marigo P., Girardi L., 2007, *A&A*, 469, 239

Marigo P., Girardi L., Bressan A., Groenewegen M. A. T., Silva L., Granato G. L., 2008, *A&A*, 482, 883

McClintock T. et al., 2019, *MNRAS*, 482, 1352

Medezinski E. et al., 2018, *PASJ*, 70, S28

Melchior P. et al., 2017, *MNRAS*, 469, 4899

Miralda-Escude J., 1991, *ApJ*, 370, 1

Miyatake H. et al., 2019, *ApJ*, 875, 63

Moraes B. et al., 2014, *Rev. Mex. Astron. Astrofis. Ser. Conf.*, 44, 202

Mulroy S. L., McGee S. L., Gillman S., Smith G. P., Haines C. P., Démoclès J., Okabe N., Egami E., 2017, *MNRAS*, 472, 3246

Murata R., Nishimichi T., Takada M., Miyatake H., Shirasaki M., More S., Takahashi R., Osato K., 2018, *ApJ*, 854, 120

Murata R. et al., 2019, *PASJ*, 71, 107

Navarro J. F., Frenk C. S., White S. D. M., 1996, *ApJ*, 462, 563

Niemiec A. et al., 2017, *MNRAS*, 471, 1153

Nishizawa A. J. et al., 2018, *PASJ*, 70, S24

Noh Y., Cohn J. D., 2012, *MNRAS*, 426, 1829

Oguri M., 2014, *MNRAS*, 444, 147

Oguri M. et al., 2018, *PASJ*, 70, S20

Okabe N., Smith G. P., 2016, *MNRAS*, 461, 3794

Overzier R. A., 2016, *A&AR*, 24, 14

Palmese A. et al., 2020, *MNRAS*, 493, 4591

Penna-Lima M., Makler M., Wuensche C. A., 2014, *J. Cosmol. Astropart. Phys.*, 5, 039

Pereira M. E. S. et al., 2018, *MNRAS*, 474, 1361

Pillepich A. et al., 2018, *MNRAS*, 475, 648

Planck Collaboration XXIV, 2016, *A&A*, 594, A24

Prat J. et al., 2018, *Phys. Rev. D*, 98, 042005

Rakos K. D., Schombert J. M., 1995, *ApJ*, 439, 47

Rozo E., Rykoff E. S., 2014, *ApJ*, 783, 80

Rozo E. et al., 2010, *ApJ*, 708, 645

Rozo E., Bartlett J. G., Evrard A. E., Rykoff E. S., 2014, *MNRAS*, 438, 78

Rykoff E. S. et al., 2014, *ApJ*, 785, 104

Rykoff E. S. et al., 2016, *ApJS*, 224, 1

Salpeter E. E., 1955, *ApJ*, 121, 161

Sampaio-Santos H. et al., 2020, preprint ([arXiv:2005.12275](https://arxiv.org/abs/2005.12275))

Sánchez-Blázquez P. et al., 2006, *MNRAS*, 371, 703

Shan H. et al., 2017, *ApJ*, 840, 104

Sheldon E., 2015, NGMIX: Gaussian Mixture Models for 2D Images, Astrophysics Source Code Library, record ascl:1508.008

Sheldon E. S., Huff E. M., 2017, *ApJ*, 841, 24

Sheldon E. S. et al., 2001, *ApJ*, 554, 881

Sheldon E. S. et al., 2004, *AJ*, 127, 2544

Simet M., McClintock T., Mandelbaum R., Rozo E., Rykoff E., Sheldon E., Wechsler R. H., 2017, *MNRAS*, 466, 3103

Simha V., Weinberg D. H., Conroy C., Dave R., Fardal M., Katz N., Oppenheimer B. D., 2014, preprint ([arXiv:1404.0402](https://arxiv.org/abs/1404.0402))

Sinha M., Garrison L., 2017, Corrfunc: Blazing Fast Correlation Functions on the CPU, Astrophysics Source Code Library, record ascl:1703.003

Sommariva V. et al., 2014, *A&A*, 571, A99

Springel V., 2005, *MNRAS*, 364, 1105

Sunayama T. et al., 2020, *MNRAS*, 496, 4468

The Dark Energy Survey Collaboration, 2005, preprint ([astro-ph/0510346](https://arxiv.org/abs/astro-ph/0510346))

The Dark Energy Survey Collaboration, 2016, *MNRAS*, 460, 1270

Varga T. N. et al., 2019, *MNRAS*, 489, 2511

Voit G. M., 2005, *Rev. Mod. Phys.*, 77, 207

von der Linden A. et al., 2014a, *MNRAS*, 439, 2

von der Linden A. et al., 2014b, *MNRAS*, 443, 1973

Wechsler R. H., Tinker J. L., 2018, *ARA&A*, 56, 435

Wen Z. L., Han J. L., 2015, *ApJ*, 807, 178

White M. et al., 2011, *ApJ*, 728, 126

Wiesner M. P., Lin H., Soares-Santos M., 2015, *MNRAS*, 452, 701

Wojtak R. et al., 2018, *MNRAS*, 481, 324

Wright C. O., Brainerd T. G., 2000, *ApJ*, 534, 34

Yang X., Mo H. J., van den Bosch F. C., Jing Y. P., Weinmann S. M., Meneghetti M., 2006, *MNRAS*, 373, 1159

Zhang Y. et al., 2019a, *MNRAS*, 487, 2578

Zhang Y. et al., 2019b, *ApJ*, 874, 165

Zitrin A., Bartelmann M., Umetsu K., Oguri M., Broadhurst T., 2012, *MNRAS*, 426, 2944

Zuntz J. et al., 2018, *MNRAS*, 481, 1149

<sup>9</sup>Center for Cosmology and Astro-Particle Physics, The Ohio State University, Columbus, OH 43210, USA

<sup>10</sup>Department of Astronomy, University of California, Berkeley, 501 Campbell Hall, Berkeley, CA 94720, USA

<sup>11</sup>Santa Cruz Institute for Particle Physics, Santa Cruz, CA 95064, USA

<sup>12</sup>Institut de Física d'Altes Energies (IFAE), The Barcelona Institute of Science and Technology, Campus UAB, E-08193 Bellaterra (Barcelona), Spain

<sup>13</sup>Department of Physics, Stanford University, 382 Via Pueblo Mall, Stanford, CA 94305, USA

<sup>14</sup>Kavli Institute for Particle Astrophysics and Cosmology, Stanford University, PO Box 2450, Stanford, CA 94305, USA

<sup>15</sup>SLAC National Accelerator Laboratory, Menlo Park, CA 94025, USA

<sup>16</sup>Département de Physique Théorique and Center for Astroparticle Physics, Université de Genève, 24 quai Ernest Ansermet, CH-1211 Geneva, Switzerland

<sup>17</sup>Department of Physics and Astronomy, University College London, Gower Street, London WC1E 6BT, UK

<sup>18</sup>Department of Physics, ETH Zurich, Wolfgang-Pauli-Strasse 16, CH-8093 Zurich, Switzerland

<sup>19</sup>Department of Physics, The Ohio State University, Columbus, OH 43210, USA

<sup>20</sup>Department of Physics and Astronomy, University of Pennsylvania, Philadelphia, PA 19104, USA

<sup>21</sup>Department of Physics and Astronomy, Stony Brook University, Stony Brook, NY 11794, USA

<sup>22</sup>Institute for Astronomy, University of Edinburgh, Edinburgh EH9 3HJ, UK

<sup>23</sup>Cerro Tololo Inter-American Observatory, NSF's National Optical-Infrared Astronomy Research Laboratory, Casilla 603, La Serena, Chile

<sup>24</sup>Departamento de Física Matemática, Instituto de Física, Universidade de São Paulo, CP 66318, São Paulo, SP 05314-970, Brazil

<sup>25</sup>Laboratório Interinstitucional de e-Astronomia – LIneA, Rua Gal. José Cristino 77, Rio de Janeiro, RJ 20921-400, Brazil

<sup>26</sup>Instituto de Física Teórica UAM/CSIC, Universidad Autónoma de Madrid, E-28049 Madrid, Spain

<sup>27</sup>CNRS, UMR 7095, Institut d'Astrophysique de Paris, F-75014 Paris, France

<sup>28</sup>Sorbonne Universités, UPMC Univ Paris 06, UMR 7095, Institut d'Astrophysique de Paris, F-75014 Paris, France

<sup>29</sup>Department of Physics and Astronomy, University of Sussex, Pevensey Building, Brighton BN1 9QH, UK

<sup>30</sup>Jodrell Bank Center for Astrophysics, School of Physics and Astronomy, University of Manchester, Oxford Road, Manchester M13 9PL, UK

<sup>31</sup>Instituto de Astrofísica de Canarias, E-38205 La Laguna, Tenerife, Spain

<sup>32</sup>Departamento Astrofísica, Universidad de La Laguna, E-38206 La Laguna, Tenerife, Spain

<sup>33</sup>Department of Astronomy, University of Illinois at Urbana-Champaign, 1002 W. Green Street, Urbana, IL 61801, USA

<sup>34</sup>National Center for Supercomputing Applications, 1205 West Clark Street, Urbana, IL 61801, USA

<sup>35</sup>INAF–Osservatorio Astronomico di Trieste, via G. B. Tiepolo 11, I-34143 Trieste, Italy

<sup>36</sup>Institute for Fundamental Physics of the Universe, Via Beirut 2, I-34014 Trieste, Italy

<sup>37</sup>Observatório Nacional, Rua Gal. José Cristino 77, Rio de Janeiro, RJ 20921-400, Brazil

<sup>38</sup>Department of Physics, IIT Hyderabad, Kandi, Telangana 502285, India

<sup>39</sup>Faculty of Physics, Ludwig-Maximilians-Universität, Scheinerstr 1, D-81679 Munich, Germany

<sup>40</sup>Institut d'Estudis Espacials de Catalunya (IEEC), E-08034 Barcelona, Spain

<sup>41</sup>Institute of Space Sciences (ICE, CSIC), Campus UAB, Carrer de Can Magrans, s/n, E-08193 Barcelona, Spain

<sup>42</sup>Department of Astronomy, University of Michigan, Ann Arbor, MI 48109, USA

<sup>43</sup>School of Mathematics and Physics, University of Queensland, Brisbane, QLD 4072, Australia

<sup>44</sup>Center for Astrophysics | Harvard & Smithsonian, 60 Garden Street, Cambridge, MA 02138, USA

<sup>45</sup>Australian Astronomical Optics, Macquarie University, North Ryde, NSW 2113, Australia

<sup>46</sup>Lowell Observatory, 1400 Mars Hill Rd, Flagstaff, AZ 86001, USA

<sup>47</sup>George P. and Cynthia Woods Mitchell Institute for Fundamental Physics and Astronomy, and Department of Physics and Astronomy, Texas A&M University, College Station, TX 77843, USA

<sup>48</sup>Department of Astrophysical Sciences, Princeton University, Peyton Hall, Princeton, NJ 08544, USA

<sup>49</sup>Institució Catalana de Recerca i Estudis Avançats, E-08010 Barcelona, Spain

<sup>50</sup>Institute of Astronomy, University of Cambridge, Madingley Road, Cambridge CB3 0HA, UK

<sup>51</sup>Centro de Investigaciones Energéticas, Medioambientales y Tecnológicas (CIEMAT), 28040 Madrid, Spain

<sup>52</sup>School of Physics and Astronomy, University of Southampton, Southampton SO17 1BJ, UK

<sup>53</sup>Computer Science and Mathematics Division, Oak Ridge National Laboratory, Oak Ridge, TN 37831, USA

This paper has been typeset from a TeX/LaTeX file prepared by the author.